

HIGH PRECISION CONTROL OF INTEGRATED MICROFLUIDICS FOR NANOMANUFACTURING AND FLUIDIC SAMPLING

A Thesis
Presented to
The Academic Faculty

By

Michael J. Toth

In Partial Fulfillment
of the Requirements for the Degree
Doctorate of Philosophy
in
Mechanical Engineering



George W. Woodruff School of Mechanical Engineering
Georgia Institute of Technology
May 2018

Copyright © Michael J. Toth 2018

HIGH PRECISION CONTROL OF INTEGRATED MICROFLUIDICS
FOR NANOMANUFACTURING AND FLUIDIC SAMPLING

Approved by:

Dr. YongTae Kim, Advisor
School of Mechanical Engineering
Georgia Institute of Technology

Dr. Peter Hesketh
School of Mechanical Engineering
Georgia Institute of Technology

Dr. Jun Ueda
School of Mechanical Engineering
Georgia Institute of Technology

Dr. Gang Bao
Department of Bioengineering
Rice University

Dr. Thomas Kurfess
School of Mechanical Engineering
Georgia Institute of Technology

Date Approved: April 3rd, 2018

Acknowledgements

First, I would like to express my sincere gratitude to my advisor, Dr. YongTae Kim, for his invaluable guidance and support throughout my Ph.D. He has shared his immense knowledge and extensive experience without reservation. I am profoundly thankful for his passion and encouragement and which not only guided me during my research, but also concreted my choice in profession. I greatly appreciate Dr. Kim as mentor. Without his support and the opportunities provided to me, this achievement would not have been possible, and I would not be the engineer that I am today.

I am grateful to all the former and current members of the Multiscale Biosystems & Multifunctional Biomaterials (MBMN) Lab, for their consistent support and friendship. Over the years each of you have become like family, consoling me through the rough times and celebrating through the triumphs. To all MBMN members, thank you for every moment that we shared. A special thank you to Taeyoung for helping me with simulations and to Yoshi for being the amazing friend over the years.

Finally, but my no means least, I cannot express enough in words how deeply appreciative of my family for their emotional support in my life and along the way. My mother and father, your support, love, and expertise has been invaluable into completing this degree. Lastly, my wife, Elena, you have supported me and kept my spirits alive that we could both finish our Ph.D. Without your love and support, none of this would have been possible.

TABLE OF CONTENTS

Acknowledgements.....	iii
List of Tables	vi
List of Figures.....	vii
List of Abbreviations	x
Summary.....	xi
Chapter 1 Introduction.....	1
1.1 Nanoparticle Synthesis.....	3
1.2 Microfluidic Nanoparticle Synthesis.....	5
1.2.1 Microfluidic Parallelization	7
1.3 Control Theory	8
1.3.1 Feedback Pressure Control	10
1.3.2 High-Precision Fluidic Sampling.....	12
1.4 Technical Approach	14
Chapter 2 High-Precision Feedback Pressure Control for Microfluidic Systems	16
2.1 Nonlinear Modeling	16
2.1.1 Single vs Dual Resistance Model	22
2.2 Nonlinear Simulation and PI Controller Design	24
2.3 Experimental System Performance	27
2.3.1 Pressure System Comparison.....	31
2.4 Conclusions	33
Chapter 3 Parallelized Microfluidics for Robust Nanomanufacturing	34
3.1 Swirling Microvortex Reactor.....	34
3.1.1 Pressure Control Integration and Analysis	38
3.1.2 Nanoparticle Versatility	41
3.2 Parallelized Microvortex Array.....	45
3.2.1 Fluidic Circuit Analog Modeling.....	45
3.2.2 Design Optimization	49

3.2.3 Prototyping and Fabrication.....	50
3.2.4 Robust Nanomanufacturing with Feedback Control.....	52
3.3 Conclusions	55
Chapter 4 High-Precision Feedback-Controlled Fluidic Sampling	57
4.1 Microvolumetric Sampler Development.....	57
4.1.1 Controller Development.....	60
4.1.2 System Performance	65
4.1.3 Continuous Sampling Approach	68
4.2 Application for Micro-Engineered Systems.....	70
4.2.1 Convective Flow Profiles.....	70
4.2.2 Static Membrane Mass Transport Simulations	73
4.2.3 Membrane Porosity Effect on Mass Transport	76
4.3 Conclusions	79
Chapter 5 Denouement	81
Broader Impact.....	81
References.....	84

List of Tables

Table 2.1 Parameters for Pressure System Equilibrium Point.....	23
Table 4.1 Summary of Sampling Device Modeling Parameters	62
Table 4.2 Simulated lower channel mass fraction analysis	75

List of Figures

Figure 1.1 Nanoparticle structure schematic.	5
Figure 1.2 Variable-Resistance and Variable Reservoir System Response.	12
Figure 2.1 Feedback pressure control schematic	17
Figure 2.2 Pressure control system fluidic circuit analog.....	19
Figure 2.3 Variable Resistance Model.....	21
Figure 2.4 Nonlinear Pressure Control Simulink Model	25
Figure 2.5 Discrete versus Continuous Simulation	26
Figure 2.6 Computer Schematic of Pressure Control System	27
Figure 2.7 Experimental Region of Interest	28
Figure 2.8 Experimental Evaluation of Pressure Drops	29
Figure 2.9 Experimental Evaluation of Sinusoidal Pressure Curves	30
Figure 2.10 Long-Term Pressure System Response.....	32
Figure 3.1 SMR Development.....	35
Figure 3.2 Mixing Efficiency Standard	35
Figure 3.3 SMR LPNP Production Schematic	37
Figure 3.4 SMR Experimental Nanoparticle Synthesis Validation	37
Figure 3.5 Electrical Decomposition of SMR	38
Figure 3.6 SMR Feedback Controller Performance	39
Figure 3.7 Steady-state/Transient Nanoparticle Synthesis Comparison.....	40
Figure 3.8 SMR Synthesized eHNP	42
Figure 3.9 SMR Synthesized PNP.....	43
Figure 3.10 SMR Synthesized LNP.....	44

Figure 3.11 PMA Fluidic Circuit Analog Decomposition.....	46
Figure 3.12 Array Size Sensitivity on Design Criteria	48
Figure 3.13 Reactors per Array Size.....	48
Figure 3.14 PMA Computational Fluid Dynamic Simulations	49
Figure 3.15 PMA Modeling Analysis.....	50
Figure 3.16 Polydimethylsiloxane PMA Prototype Schematic	51
Figure 3.17 Robust PMA Design.....	52
Figure 3.18 Feedback Control PMA Integration	53
Figure 3.19 Controlled LPNP Synthesis on PMA	54
Figure 3.20 LPNP Synthesis Comparison of SMR vs PMA	55
Figure 4.1 Sampling Device Schematic and Integration	58
Figure 4.2 Integrated Organ-on-a-chip Schematic	59
Figure 4.3 Sampling Device Operation Schematic.....	59
Figure 4.4 Microvolumetric sampler Mathematical Constraints.....	60
Figure 4.5 Motor Control Block Diagram	61
Figure 4.6 Simulated Sampling Device Motor Control.....	63
Figure 4.7 Experimental Sampling Device Controller Performance	64
Figure 4.8 Sampling System Controller Comparison.....	65
Figure 4.9 Sampling Fluidic Time Delay Diagram	66
Figure 4.10 Sampling Device Accuracy Based on Flow Rate.....	67
Figure 4.11 Microvolumetric Sampler Plasma Oxidation Performance	67
Figure 4.12 Continuous Sampling Circuit Diagram	68
Figure 4.13 Continuous Sampling Time Differential	69

Figure 4.14 Simulated Continuous Microvolumetric Sampler Design	69
Figure 4.15 Sampling Convective Experiment Schematic	71
Figure 4.16 Flow Rate Comparison of Convective Experiment.....	72
Figure 4.17 Effect of Pulse Duration on Drug/Compound Concentration	73
Figure 4.18 Static Membrane Diffusion Simulation.....	74
Figure 4.19 Transient Membrane Mass Transport	75
Figure 4.20 Steady-State Membrane Mass Transport	76
Figure 4.21 Membrane Porosity Mass Transport Simulation Schematic	77
Figure 4.22 Lower Channel Steady-State Mass Fraction	78
Figure 4.23 Lower Channel Mass Fraction Distribution	79

List of Abbreviations

Acetonitrile	ACN
Computational Fluid Dynamics	CFD
Dynamic Light Scattering	DLS
Engineered High Density Lipoprotein	eHNP
Ethanol	EtOH
Lipid Polymer Nanoparticle.....	LPNP
Liposome.....	LNP
Nanoparticle	NP
Parallelized Microvortex Array	PMA
Polydispersity Index.....	PDI
Polymeric Nanoparticle	PNP
Reynolds Number	Re
Transmission Electron Microscopy	TEM

Summary

Combining the engineering principles of system dynamics and control theory with biological applications of nanoparticle synthesis and organ-on-a-chip, this work aims to advance these areas of research by developing precision control systems for high-throughput synthesis and high-precision sampling, respectively. A high-precision feedback pressure control system is developed to regulate the inlet pressure of microfluidic device, controlling the flow rate, for high precision nanoparticle synthesis. Mathematical derivation and experimental validation of the pressure system are discussed, with performance achieving less than 0.5% steady-state error for long term experimental duration (3 hours) and 0.3 second settling time. The pressure control system is integrated with the development of a parallelized microvortex array, designed to increase the multiplicity of microfluidic reactors in parallel for high-throughput nanoparticle manufacturing. Critical parameters (i.e., Reynolds number and precursor composition) to maintaining nanoparticle quality are assessed and factored into the development of fluidic circuit analog and computational fluid dynamic models. A robust 3-part device is fabricated for experimental validation of the design methodology. Lastly, the development of a tunable low-cost (\$250) high-precision sampling device with settling times less than 0.3 seconds, overshoot less than 2%, and zero steady-state error. Mathematical derivation of the controller and microvolumetric sampler constraints are discussed. The performance is experimentally validated through various input flow profiles. The entirety of this work can potentially advance not only the clinical translation of nanoparticles and biological sampling, but can additionally create high-precision experimentation in a variety of fields such as chemistry, life sciences, energy conversion, and defense.

Chapter 1 Introduction

A number of nanoparticles (NPs) have been developed for targeted delivery of therapeutic and imaging agents for the treatment and diagnosis of major diseases including cancer [1-3], cardiovascular disease [4, 5], diabetes [6, 7], and Alzheimer's disease [8-10]. For a decade, only a small number of therapeutic and diagnostic (theranostic) NPs have been approved by the FDA [11, 12]. This low success rate in the “bench to bedside” translation is due in part to low reproducibility of desired properties or efficacies of developed nanomedicines in prescreening processes from in vitro testing to in vivo validation [13]. With pharmaceutical and biomedical industries acknowledging the challenges in scaling the production of NPs, there is a growing need for the development of robust technology for nanomedicine manufacturing [14-16]. The expanding field of microfluidics has been utilized in the development of NPs [17, 18], and developed as a platform to accelerate the translation of nanomedicines in response to this need [14].

Microfluidic platforms provide controllable flow patterns with tunable characteristic mixing times on the millisecond to microsecond scale that can be used for diffusive or convective mixing mechanisms [19-27]; however, these microfluidics-based NP syntheses have been largely limited to small-scale production of specific single component NPs with considerably less research on the scale-up applications [14-16]. Numerous studies have demonstrated that microfluidic synthesis produces narrower NP size distributions (i.e., high size uniformity) than those of conventional multi-step benchtop synthesis methods [28, 29], but the production rate remains restricted by a low throughput (up to a few grams per hour) [30, 31]. A recent approach using a turbulent impinging jet flow to synthesize polymeric NPs in a single device achieved a much higher production rate on the order of

kg/d [32]; however, optimization process of multicomponent NP synthesis in turbulent flow at macroscale remains impractical due to waste of costly precursors, and the effect of the high shear rate generated by turbulent flow on the stability or degradation of precursors remains to be investigated. This challenge underscores the importance of microfluidic parallelization technology that preserves the advantages of the microscale reaction by maintaining the characteristic mixing times on the millisecond to microsecond scale and the consistency of reactor conditions. Although several microfluidic parallelization approaches have been previously introduced using simple diffusive mixing to improve production rates from mg/d to g/d [15, 33-35], no reliable and practical approach has been established for scalable manufacturing of NPs to an industrially relevant level, such as attaining a production rate on the order of kg/d [12, 15, 36-38].

This challenge is multifaceted but is largely due to the ambiguity that still surrounds the mechanisms of flow-induced NP formation and the reliance of microfluidic synthesis on conventional (open-loop) programmable syringe pumps. Microfluidic synthesis of NPs for parallelization rely on flow dynamic similarity across devices; however, to create a robust parallelized array, synthesis parameters affecting NP quality need to be optimized. Syringe pumps are not a robust methodology for scalable manufacturing of NPs due to several problems including the limited syringe size and the open-loop control-based operation that is unable to compensate for unexpected disturbances in the manufacturing process leading to non-robust production operations.

In addition to addressing high-throughput nanoparticle synthesis, this work aims to apply engineering principles to biological systems with the development of a high-precision sampling device for biological applications (*e.g.*, organ-on-a-chip).

Discretization of biological samples, where specific volumes of a system are isolated for analysis, is an essential component of biological research for organ-on-a-chip [39-43], chemical syntheses [44, 45], and drug discovery [46-48]. Conventionally, experimental sampling, in a laboratory setting, relies on both the temporal and volumetric accuracy of the user, a potential source of error and variations across repeated experimentation. By applying the principles of control theory, a high-precision sampling device can be developed to eliminate the potential sources of error. This proposed device will help to automate the laboratory setting, allowing for more consistent and repeatable experiments.

Based on the challenges presented and for the understanding of this work, the principles of NP synthesis, microfluidics, and control theory are discussed.

1.1 Nanoparticle Synthesis

A wide range of NPs have been developed including quantum dots [49], gold NPs [50, 51], iron-oxide NPs [52], high-density lipoproteins[53], liposomes [54, 55], polymeric NPs [56, 57], and lipid-polymer NPs (LPNPs) [58]. NPs have been used in a variety of applications such as drug delivery, fluorescent labeling, magnetic resonance imaging (MRI), contrast enhancement, and tissue engineering [59, 60]. Primarily, this work focuses on the development of NPs for the delivery of targeted therapeutics. Liposomes (LNPs) have been used as drug carriers due to their biocompatibility, tunable surface chemistry, and ability to protect drugs from degradation [1, 61]. However, LNPs have a low drug encapsulation efficiency, thus limiting their effectiveness as drug carriers [62]. Polymeric NPs (PNPs) provide the advantage hydrophobic drug encapsulation [63] with high drug encapsulation efficiency [1, 64]. However, without PEGylation of PNPs (the incorporation of polyethylene glycol (PEG)), the hydrophobic PNPs are rapidly cleared from blood

circulation due to foreign body immune response [65]. PEGylation enables longer circulation time by reducing adverse immune responses (i.e. phagocytosis), lowers renal clearance by increasing particle size, increases solubility and particle stability as well as enhances charge chemistry of NPs for cellular uptake [66, 67].

LPNPs were chosen as a platform for the development and optimization of the swirling microvortex reactor (SMR) because LPNPs leverage the advantages and mitigate the disadvantages of both polymeric NPs and liposomes (Figure 1.1) by incorporating a polymeric core within a PEGylated lipid shell [68]. Although this work primarily focuses on the development of LPNP, both PNPs and LNPs are still widely researched due to their unique properties and are examined on the developed platform. Briefly, LPNPs are conventionally synthesized by the rapid mixing of a polymer (e.g. poly(D,L-lactic-co-glycolic acid) (PLGA)) in an organic solvent (e.g. acetonitrile) with a lipid (e.g. 1,2-dipalmitoyl-sn-glycero-3-phosphocholine (DPPC) and 1,2-Distearoylsn- glycero-3-phosphoethanolamine-N-[methoxy(polyethylene glycol)-2000] (DSPE-PEG)) in aqueous ethanol through a single or two-step process [69]. The resulting synthesized LPNPs can be evaluated for size uniformity with dynamic light scattering (DLS) and morphological characteristics with transmission electron microscopy (TEM). Due to the versatility of LPNPs, this work focuses on leveraging microfluidic devices to achieve high quality (i.e. low polydispersity) LPNPs at large-scale manufacturing. Synthesis of additional multicomponent NPs (e.g. engineered high-density lipoproteins, liposomes, and polymeric NPs) will be explored following the successful manufacturing of LPNPs.

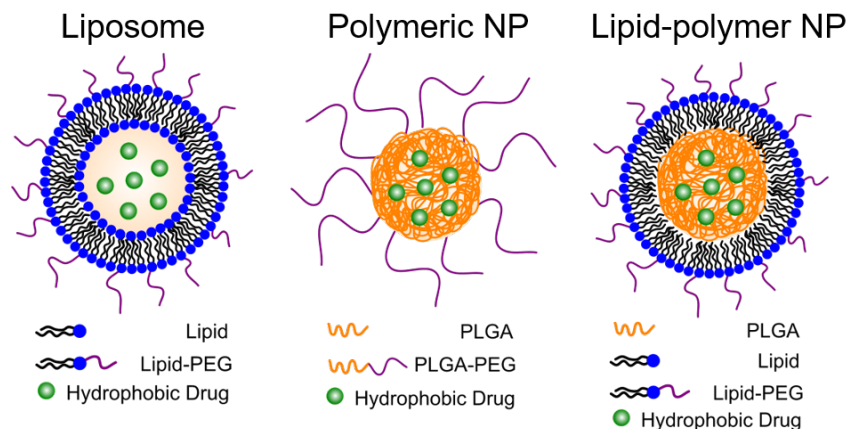


Figure 1.1 Nanoparticle structure schematic.

1.2 Microfluidic Nanoparticle Synthesis

Over the last decade, there has been an increase in the development of microfluidic technologies for a variety of applications including life sciences [70], chemistry [71, 72], energy conversion [73], and defense [74]. Microfluidic devices are conventionally fabricated by a combination of photolithography and soft lithography. Photolithography involves the deposition of a photosensitive compound on a silicon wafer to create a mold. The compound is cured through high-intensity light exposure through a mask to produce a desired structure. Soft lithography involves applying and curing polydimethylsiloxane (PDMS) over the mold to imbed the desired structure. The resulting PDMS, containing the microfluidic structure, can be bonded to glass through oxidative plasma cleaning to create a finalized microfluidic device.

Prior to the development of microfluidic technology, NP synthesis relied on “bench top” synthesis in which nanoprecipitation occurs through agitation from a stirrer or vortexer [75, 76]. Although a well-trained practitioner can batch produce NPs with homogenous size distributions, microfluidics provides a means for a controllable, well-

characterized platform for consistent and continuous production of homogenous NPs. The first development of microfluidic technology to be applied to NP synthesis was “droplet” technology [77, 78]. The droplet is formed by the combination of insoluble solutions (e.g., water and oil) to create discretized droplets in a microfluidic channel. These discretized solutions move along the channel experiencing Dean’s flow, causing internal droplet flow and mixing of species within the droplet [79-81]. By having multiple reagents in a single droplet, rapid mixing can occur via continuous rotation of the droplet forming NPs. Microfluidics moved toward the development of continuous flow approaches with the development of hydrodynamic flow focusing [19, 82, 83], where mixing is diffusion dominated, generally long time constants, by minimizing the distance between the reagents. This pattern resolved the understanding of the fluid pattern by reducing the system to laminar flow, but it remains limited in the production rate of NPs (on the order of mg/hr).

To overcome this limitation, convection based microfluidics were developed using microvortices [25, 84] and swirling flows [31]. Convective mixing ($Re > 100$) allows for characteristic mixing times (1), where D represents the hydrodynamic diameter and v represents the fluid velocity, to remain smaller than diffusion times (2), where R represents the radius and D_c represents the diffusion constant (on order of $1E-9$). By increasing the velocity of the fluid (proportional to the Reynolds number) above (3), the convective mixing constant remains lower than the diffusive constant. Convective mixing therefore allows for a controlled, rapid mixing interface between NP precursor solutions coupled with hydrodynamic flow focusing of the precursors, allowing for further increase of NP production rates (on the order of g/hr).

$$\tau_{Mix} = \frac{D}{v} \quad (1)$$

$$\tau_{Diff} = \frac{2R}{D_c} \quad (2)$$

$$v > \frac{2D_c}{R} \quad (3)$$

While this is a significant advancement in NP technology, the microfluidic device consists of only a singular module, thus limiting the overall production rate of NPs. To translate this technology to a sustainable manufacturing level, larger scale integration is required [13, 14, 18, 63]. To increase production, two methodologies are considered: scale-up and parallelization. Scaling of a microfluidic device can achieve larger production; however, the advantage of microscale interactions allowing for improved polydispersity are potentially compromised, limiting the magnitude of scaling that can be achieved. Parallelization of microfluidics utilizes the standard manufacturing technique of simultaneous production while maintaining quality standards; however, requires a complex connective network to ensure reaction consistency.

1.2.1 Microfluidic Parallelization

Developments in scalable synthesis include the parallelization of droplet microfluidics [33, 85, 86] and hydrodynamic flow focusing microfluidics [15]. Work by Nisisako [33, 87] demonstrates the increase in droplet production with the development of a 128 array of droplet microfluidics. This device demonstrated the use of a common inlet and outlet for all reactors, further explored by Mulligan [35], reducing the complexity of the design for operation while achieving simultaneous across all reactors. Romanowsky [34] demonstrated the development of a parallelized device through the use of a fluidic circuit analog [88], a critical tool to be predict flow consistency across all microfluidic reactors,

to be further explored with this work. These droplet microfluidic platforms, not necessarily designed for NP synthesis, demonstrated the development of parallelized microfluidic for industrial use, providing key tools for designing; however, remain inherently limited in production rate with a Reynolds number ($Re \ll 1$), a measure of flow viscous forces versus inertial forces. Lim [15] developed a parallelized platform of hydrodynamic flow focusing microfluidics combining 8 diffusive microfluidic devices for simultaneous polymeric NP synthesis. While this methodology can maintain homogeneous NP distribution across all devices, it remains limited in overall production of NPs (mg/hr at $Re \ll 1$) and the complexity of fabrication may potentially limit accessibility for industrial applications. Alternatively to parallelization, a ultra-high throughput (on the order of kg/d) of NPs by using turbulent flow was developed by Lim [32]. However, the high shear rates used in this turbulent flow can potentially cause instability or degradation of costly therapeutic agents potentially leading to unpredictable variations in NP properties and decreased therapeutic effect.

Parallelization of convective microfluidic devices provides an unexplored opportunity for industrial scale synthesis (on the order of kg/hr) of multicomponent and multifunctional NPs. This work demonstrates the development of a parallelized microvortex array (PMA) for mass production of multicomponent therapeutic NPs by assessing and minimizing critical parameters of single-chip based synthesis with electrical fluidic analog modeling.

1.3 Control Theory

A combination of engineering and mathematics, control theory deals with the behavior of dynamic models based on the inputs to the system. A physical system (mechanical, fluidic, electrical, etc.) is first modeled and characterized with a set of governing

differential equations. Through the development of the model there is a loss of information, based on model assumptions, reducing model accuracy. Computationally evaluation of the model is used to predict output state variables based on input(s) to the system. Control theory can be utilized to shape the output to achieved desired performance characteristics (steady-state error, settling time, rise time, overshoot, etc.). Within control theory, there are two main divisions: open-loop control and closed-loop control. Open-loop control uses amplifier without feedback regulation to provide fast performance. However, it requires a well understood model for the dynamics of the complete system to provide high performance, not generally suited for nonlinear systems. Without the addition of feedback control, external disturbances cannot be mitigated, resulting in output oscillations and error. Closed-loop control performance is generally slower when compared to open-loop, but it provides the distinct advantage of minimizing/eliminating error from the reference signal through sensory feedback and remains a more robust system than open-loop control. External disturbances can be mitigated as the input to the system is continually updated based on the current state of the system relative to the desired reference. Dynamic models of the system do not need to be fully understood to implement closed-loop control for high performance, but controller design remains a large contributing factor to the stability of the system. Instability can occur in the system if the controller is poorly designed, leading to device malfunction and/or failure. Additionally, the design of linear controllers (e.g., proportional-integrative-derivative or lead/lag compensator) can be used to control nonlinear systems with the addition feedback control, allowing for simplistic controller architecture and design to complex systems.

1.3.1 Feedback Pressure Control

In the context of this work, the method of fluid flow through microfluidic device is addressed by controlling the pressure differential across the device. Most microfluidic systems commonly use syringe pumps to create laminar flows within microfluidic devices. These pumps largely use step motors that may inadvertently generate pulsatile flow [89, 90] and rely on an open-loop based operation which culminates in non-robust control of flow rates and the inability to respond to disturbances such as unexpected pressure variation [91]. The hydrodynamic resistance of microfluidics (order of $1\text{E}+15 \text{ Pa} \frac{\text{s}}{\text{m}^3}$) contributes to syringe pumps exhibiting long transient times [92, 93], potentially limiting applications.

These syringe pump challenges have been partially addressed [94-99]; however, syringe pump systems remain limited by maximum syringe size and motor speed, potentially limiting manufacturing levels of NPs on parallelized microfluidics. In contrast to syringe pump systems, pressure modulation mechanisms provide variable reservoir sizes and high-pressurized sources, allowing for long-term duration at high-throughput, compared to syringe pumps. A variety of methodologies have been developed [100-105] to control flow, with applications to microfluidics.

Here, a previously developed pressure modulation mechanism allowing long-term (duration of 15 hours) and high-speed control of microfluidic flows [106, 107] is analyzed. The inlet pressure of a microfluidic device was controlled by modulating a variable resistance and a flexible reservoir in a fluidic network between a fluidic precursor reservoir to a microfluidic device. The flexible reservoir allows for an alternative fluidic drainage to the microfluidic device, rapidly decreasing the inlet pressure to the device, which improves settling time by over 500% compared to single variable resistance only model. The flexible

reservoir contributes to both an increase and decrease in pressure as the tube is compressed and released. When maintaining constant pressure, it can be observed that the flexible reservoir contributes to the steady-state inlet pressure. During long-term experimentation, when the finite volume of the flexible reservoir is exhausted, by a completely compressed tube, the pressure can no longer be maintained and decreases. The system compensates by increasing the pressure with a pressurized reservoir, causing a large overshoot and releasing the reservoir. This process becomes cyclic leading to the generation of an oscillatory flow profile, undesirable for high precision microfluidic NP synthesis, maintained within 2.5% steady-state error (Figure 1.2).

Although the coupled variable resistance and flexible reservoir allowed for rapid pressure variations, the inability to independently control may limit performance. To overcome this limitation and address the oscillatory behavior, this work will demonstrate a dual variable resistance model with independent control of compression/release of microfluidic tubing. This will eliminate the oscillatory flow present in the previous model and be coupled with the PMA for high-precision NP manufacturing.

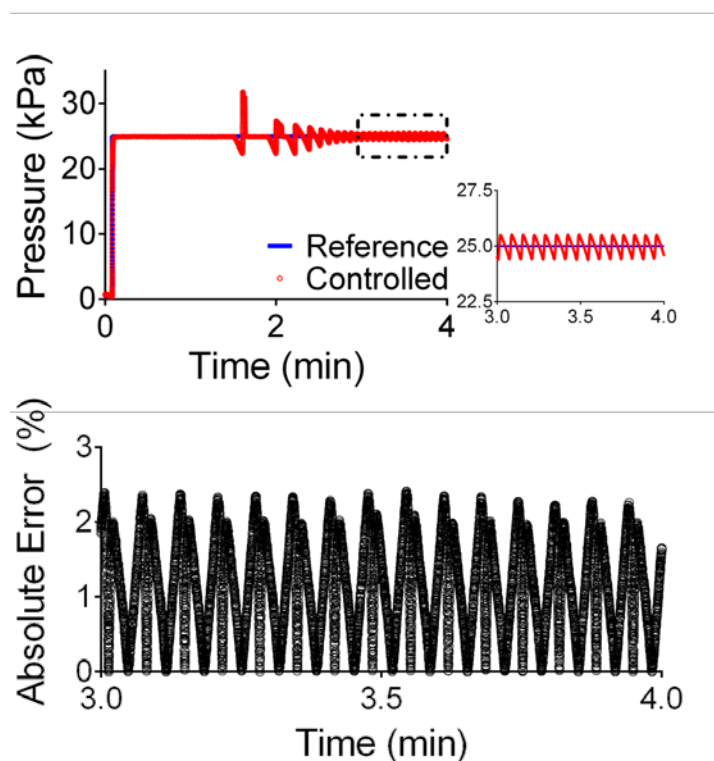


Figure 1.2 Variable-Resistance and Variable Reservoir System Response.

1.3.2 High-Precision Fluidic Sampling

Discretization of biological samples, where specific volumes of a system are isolated for analysis, is an essential component of biological research for organ-on-a-chip [39-43, 108], chemical syntheses [44, 45], and drug discovery [46-48]. Conventionally, experimental sampling, in a laboratory setting, relies on both the temporal and volumetric accuracy of the user, a potential source of error and variations across repeated experimentation. Microfluidics has become a recent approach to create an on-chip sample discretization using polydimethylsiloxane (PDMS) microfluidic valves controlled through a pressure differential [103, 109-112]. Scalability of pressure controlled microfluidic valves has been demonstrated [79, 113, 114]; however, scaling the multiplicity of

discretized samples requires an increase in pressure controlled microfluidic valves and subsequent pressure regulation apparatus, increasing both overall complexity and expense.

Microfluidic droplet generators [77, 78, 115-118] have demonstrated the ability to discretize fluidic samples by introducing an immiscible fluid to sample stream, segmenting the flow. The use of these devices requires continuous measurement devices (e.g., flow cytometer) for analysis and requires precision flow control for proper operation. Additionally, the scalability of droplet generators [33, 87] requires the complex understanding of parallelization [15, 34, 84] to design and ensure similarity between the multiplicity of sample volume and temporal differentials. Overcoming the necessity for continuous measurement devices, recent approaches have demonstrated nanoliter sampling [119] and picoliter sampling [120] to separate fluid into discretized wells. The mathematical complexity of the design and nanoliter and picoliter sampling may preclude the use with microfluidic systems (e.g., organ-on-a-chip devices), requiring system adaptability and microliter sampling [39-43, 108].

The use of sampling can be used in a broad range of applications from measuring cellular expression to nanoparticle fluorescent. Critical to the analysis of organ-on-a-chip systems is the application of physiologically relevant drug/compound dosages. Improper dosages can lead to nonphysiologically relevant cellular responses or cause apoptosis/necrosis, skewing result. To better understand the dosage levels applied to the cells, sampling can be applied to map the dosage distribution overtime for both static and dynamics drug/compound dosages.

This works presents an approach that integrates the use of feedback control with a tunable microvolumetric sampler device for a low-cost high-precision sampling

performance of biological micro-engineered systems. The motor dynamics are first modeled and experimentally validated the design of the rotational feedback controller with settling times less than 0.3 seconds, overshoot less than 2%, and zero steady-state error. The design constraints of the microvolumetric sampler are discussed, including multiplicity and size of sample effect on the controller implementation. After outlining the performance of the device, the microvolumetric sampler device is integrated with the organ-on-a-chip platform [43] to demonstrate the robust high-precision sampling of drug dosages. The analysis of cellular drug/compound loading is extended by computationally assessing the effect of membrane porosity.

1.4 Technical Approach

The primary purpose of this work is to develop a large scale parallelized array of swirling microvortex reactors (SMRs) coupled with high-precision pressure control for robust NP manufacturing. The resulting technology should accelerate the clinical translation of NPs by providing a means to mass produce high quality nanotherapeutics for testing. The following chapters will explore development of this technology by addressing the following goals:

1. Development of a high precision, high-throughput, and long-term experimentation pressure control system of microfluidic platforms
2. Development of a parallelized microvortex array (PMA) system for NP manufacturing.
3. Development of automated experimental microvolumetric sampler for precision analysis.

These goals are multifaceted requiring optimization and minimization of key parameters effecting LPNP quality. The single-reactor level needs to be analyzed to maximize quality of LPNP prior to parallelization. As with most engineering problems, a single solution is rarely unique for a broad range of applications and generalization of the process come with a cost. In the case of microfluidic inlet pressure control, the design criteria of the system are set as less than 0.5s settling time, zero steady-state error, and less than 5% overshoot.

The microvolumetric sampler device is designed to overcome limitations of human variation in both time points and volume of samples. The design criteria of the microvolumetric sampler device are set to less than 0.3s settling time, zero steady-state error, and less than 2% overshoot. The overall design of the apparatus needs to be expandable to allow a multiplicity of samples as various desired volumes to increase the versatility and applications of the device.

Chapter 2 High-Precision Feedback Pressure Control for Microfluidic Systems

In this chapter, an enhanced nonlinear pressure modulation mechanism model is developed based on independent controls of dual fluidic resistances for long-term, high-speed, and high-precision (less than 0.5% steady-state error) control of the inlet pressure in microfluidic devices. Instead of using a single DC motor applied in a previous model [106, 107], dual linear actuators are implemented to achieve independent modulation of dual fluidic resistances, which provides versatile controller design and implementation. Through continuous and discrete time models (SIMULINK[®]) of the nonlinear pressure modulation mechanism, system dynamics are predicted and utilized to tune a linear controller for the system. With the tuned controller, system responses on implemented hardware are demonstrated to show the performance of the controlled system and address long-term stability of this advanced model.

2.1 Nonlinear Modeling

The pressure control system (Figure 2.1) consists of two independent variable resistances, u_{R_1} and u_{R_2} , to control the inlet pressure of a microfluidic device. These variable resistances are modulated by the displacement of two independently controlled linear actuators, inducing a compression/release of elastic tubing inducing a nonlinear change in cross-sectional area. Feedback of the microfluidic inlet pressure regulates the linear actuator displacement in response to differences from a desired reference pressure. In this pressure modulation mechanism, u_{R_1} is decreased and u_{R_2} is increased for an increase in pressure, while u_{R_1} is increased and u_{R_2} is decreased for a decrease in pressure.

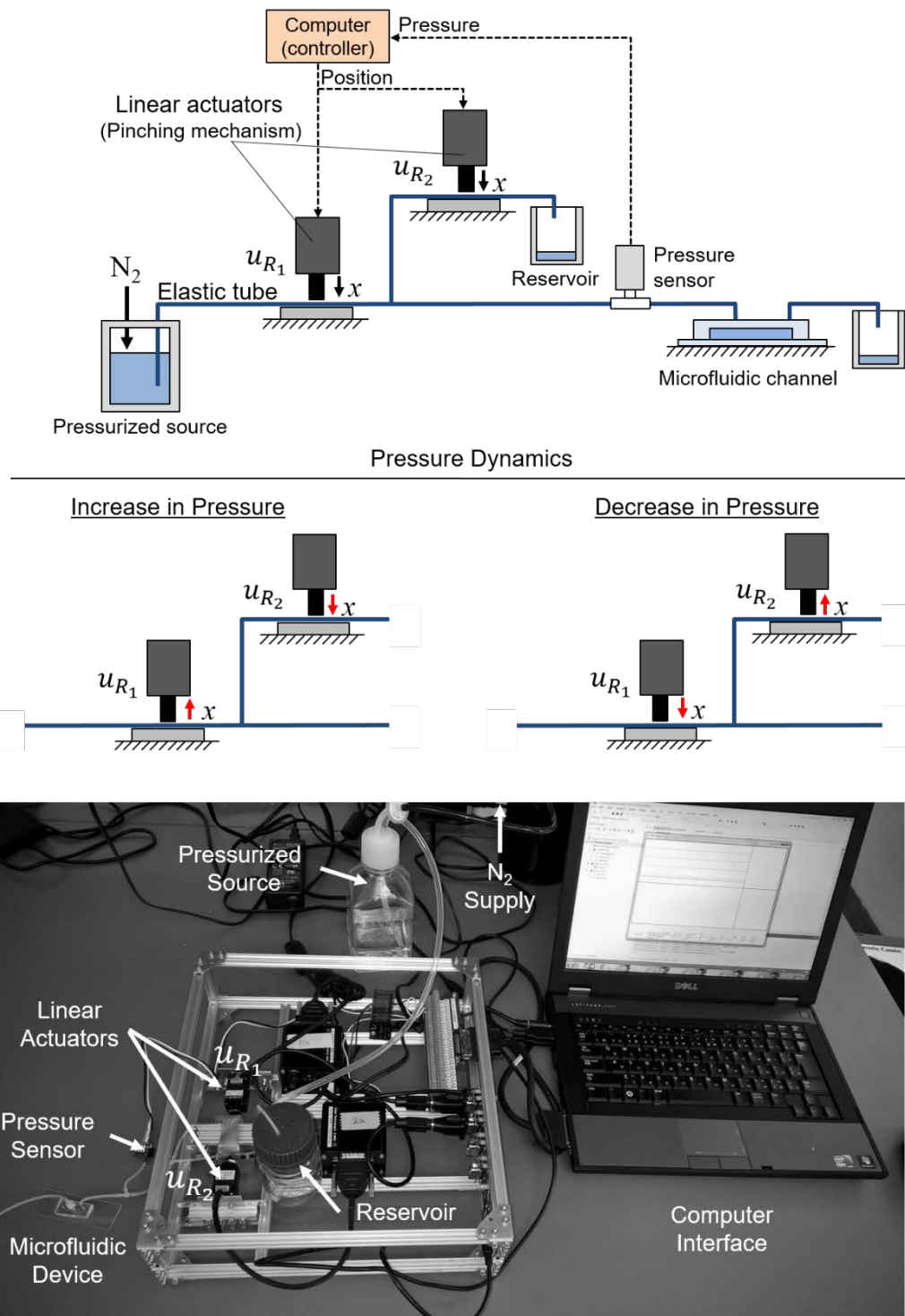


Figure 2.1 Feedback pressure control schematic

To develop a model of the pressure control system, the schematic is decomposed into a fluidic circuit analog (Figure 2.2), consisting of fluidic resistance R , fluidic capacitance C , and two variable fluidic resistances, u_{R_1} and u_{R_2} . P_r represents the reference pressure that is applied to the source. R_r represents the fluidic resistance of the connection between the source and u_{R_1} . P represents the pressure at the inlet of a microfluidic channel, which is to be controlled in the model. R_i represents the fluidic resistance of a microfluidic inlet. R_o represents the fluidic resistance of a microfluidic outlet. It was previously shown [106] that the contribution of P_o to the change in P can be neglected if $P_o \ll P$ when the inlet resistance R_i is on the order $1E+3$ greater than R_o . In this model, the total flow q is divided into three flow rates (4).

$$q = q_{u_{R_2}} + q_C + q_{R_i} \quad (4)$$

From the fluidic circuit analog, individual flow rates for total flow (5), flow to the reservoir, $q_{u_{R_2}}$ (6), flow due to tubing capacitance, q_C (7), and flow to the microfluidic device, q_{R_i} (8), can be defined.

$$q = \frac{P_r - P}{u_{R_1} + R_r} \quad (5)$$

$$q_{u_{R_2}} = \frac{P}{u_{R_2}} \quad (6)$$

$$q_C = \frac{dP}{dt} C \quad (7)$$

$$q_{R_i} = \frac{P}{R_i} \quad (8)$$

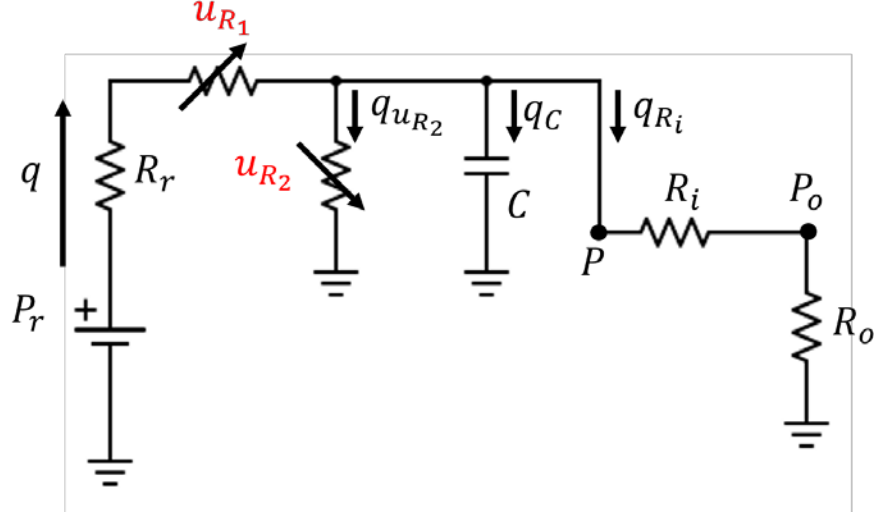


Figure 2.2 Pressure control system fluidic circuit analog

By substituting equations (5), (6), (7), and (8) into equation (4), the nonlinear dynamic model for the microfluidic inlet pressure, P , can be derived (9).

$$\frac{dP}{dt} = - \left(\frac{1}{(u_{R_1} + R_r)C} + \frac{1}{R_i C} + \frac{1}{u_{R_2} C} \right) P + \frac{P_r}{(u_{R_1} + R_r)C} \quad (9)$$

This equation represents a first-order nonlinear differential equation where the time constant can be tuned by modulating the two inputs of the independent resistances u_{R_1} and u_{R_2} . Given that each variable resistance has a lower bound, for a fully released tube, greater than 0, the dynamics of the system can be shown to be stable for all combinations of u_{R_1} and u_{R_2} by examining the equilibrium point (10).

$$P_{eq} = \frac{P_r R_i u_{R_2}}{R_i u_{R_2} + R_i (u_{R_1} + R_r) + u_{R_2} (u_{R_1} + R_r)} \quad (10)$$

By perturbing the system away from the equilibrium point by ϵ , where $\epsilon \ll 1$, the rate of change of the pressure, $\frac{dP}{dt}$, the response of the system can be examined (11). From the equation, any perturbation, either positive or negative, drives the system back towards the

equilibrium point by resulting in dP/dt opposite in sign to the perturbation, an indication of stability. This is a result of all variables within (11) remaining strictly positive values.

$$\frac{dP}{dt}(\epsilon) = - \frac{\pm \epsilon \left((R_i + R_r + u_{R_1})u_{R_2} + R_i(u_{R_1} + R_r) \right)}{u_{R_2} C R_i (u_{R_1} + R_r)} \quad (11)$$

To complete the model, the variable resistance of the tubing needs to be incorporated. When the linear actuator deforms (compresses or releases) the connective tubing to modify the fluidic resistance, the deformation of the tubing is nonlinear. By assuming a constant inner circumference of the tubing through the deformation, the nonlinearity can be approximated by using weighted averages of both circular and rectangular cross sections; the circular model is accurate near the start of tube compression (i.e., fully released) while the rectangular model is relatively accurate near the end of the tube compression (i.e., fully compressed). To estimate the deformed cross section area of the tubing, a model for the full range of the tubing deformation (Figure 2.3) was developed, through a linear combination of the resistance equations based on total displacement. The elastic tubing dilatibility was not incorporated into the model to maintain simplicity. Additionally, the mathematical derivation of an elliptical cross-sectional area is increasing complex with time-varying semi-minor and semi-major axis and does not fully define the deformed tubing shape due to the linear actuator tip geometry, therefore elliptical approaches were not considered. Although an advantage of feedback control is the elimination of the steady-state error allowing for conservative resistance estimations to achieve similar performance; by decreasing the error of the estimation, a more versatile controller can be designed to achieve desired performance.

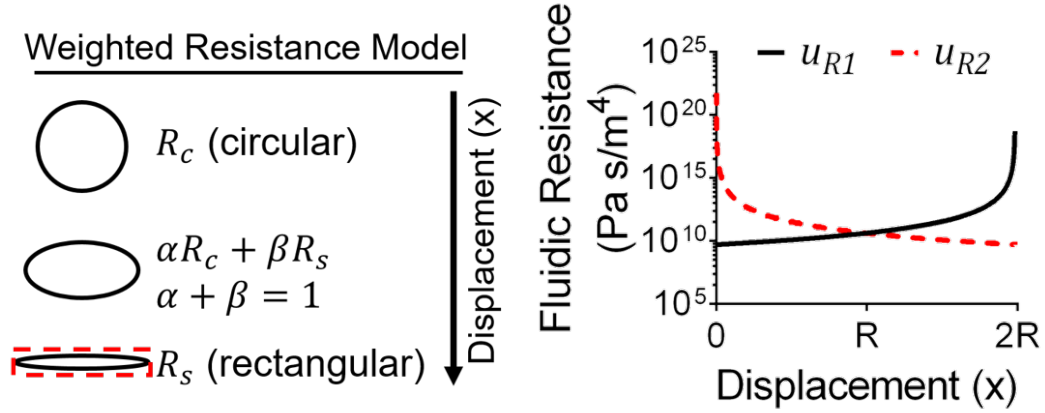


Figure 2.3 Variable Resistance Model

The mathematical equation for u_{R_1} is modeled as an open tubing (12). Where R represents the original radius of the tubing, μ represents the viscosity of the liquid, L represents the length of compression, and $h(x_1)$ (13) represents the height of the tubing (i.e. the displacement of the linear actuator subtracted from the diameter of the tubing). Similarly, the equation for u_{R_2} is modeled as a pinched tubing to reflect the resulting asymmetric motion in the pressure modulation mechanism. The equation for u_{R_2} is obtained by substituting for x_1 using the relationship defined in (14), where α is a proportional scaling constant. Using these equations, the resistance of the tube can be shown as a function of the displacement (Figure 2.3).

$$u_{R_1} = \frac{h(x_1)}{2R} \frac{8\mu L}{\pi \left(\frac{h(x_1)}{2}\right)^4} + \frac{x_1}{2R} \frac{12\mu L}{(\pi R - h(x_1))h(x_1)^3 \left(1 - \frac{0.630h(x_1)}{\pi R - h(x_1)}\right)} \quad (12)$$

$$h(x_1) = 2R - x_1 \quad (13)$$

$$x_1 = 2R - \alpha x_2 \quad (14)$$

2.1.1 Single vs Dual Resistance Model

To compare the contribution of the additional variable resistance for pressure control, the transfer function, between the inlet pressure, P , and the linear actuator displacement, x , is first constructed from state-space matrices derived through linearization of the pressure dynamic equation (9). These state-space matrices can be represented with state variables P , x and input \dot{x} (15-16).

$$\begin{bmatrix} \dot{P} \\ \dot{x} \end{bmatrix} = \begin{bmatrix} \frac{\partial F}{\partial P} & \frac{\partial F}{\partial x} \\ 0 & 0 \end{bmatrix}_{\bar{x}=x_o} \begin{bmatrix} P \\ x \end{bmatrix} + \begin{bmatrix} 0 \\ 1 \end{bmatrix} \dot{x} \quad (15)$$

$$y = [1 \ 0] \begin{bmatrix} P \\ x \end{bmatrix} \quad (16)$$

where F represents the equation of motion (9) and x_o represents the equilibrium condition (Table 2.1). By converting the linearized state-space model to an equivalent transfer function, through standard equations, and simplifying the resulting equation, the pressure dynamic transfer function is a type 0 strictly proper transfer function (17). To observe the benefits of a second variable resistor, the examination of actuator dynamics, which are congruent across each design, are excluded.

Table 2.1 Parameters for Pressure System Equilibrium Point

PARAMETERS		VALUE	UNIT
x_o	Equilibrium Actuator Position	3.9E-4	m
P_r	Source Pressure	68.9	kPa
P_o	Initial Microchannel Pressure	15.1	kPa
R_r	Upstream resistance	1.0E+10	$Pa\ s/m^3$
R_i	Microchannel Resistance	3.2E+20	$Pa\ s/m^3$
C	Microchannel Capacitance	7.6E-12	m^3/Pa
u_{R_1}	Variable Resistance 1	3.4E+9	$Pa\ s/m^3$
u_{R_2}	Variable Resistance 2	3.7E+9	$Pa\ s/m^3$
$\frac{du_{R_1}}{dx}$	Derivative of u_{R_1} w.r.t. x	2.5E+13	$Pa\ s/m^4$
$\frac{du_{R_2}}{dx}$	Derivative of u_{R_2} w.r.t. x	-2.9E+13	$Pa\ s/m^4$

$$G(s) = \frac{\frac{du_{R_1}}{dx}(x_0) \frac{P_r - P_o}{(R_r + u_{R_1}(x_0))^2} - \frac{du_{R_2}}{dx}(x_0) \frac{P_o}{u_{R_2}^2(x_0)}}{Cs + \left(\frac{1}{R_i} + \frac{1}{(R_r + u_{R_1}(x_0))} + \frac{1}{u_{R_2}(x_0)} \right)} \quad (17)$$

For a single variable resistor model, all the fluidic drainage flows through the microfluidic device (i.e., $q_{u_{R_2}} = 0$; $u_{R_2} = \infty$), where the resistance is 10-fold greater than elastic tubing. This leads to long transient time (minutes to hours) for the system to reach steady-state, which will be examined through comparison of the system time constants. The transfer function for the single variable resistance model is simply obtained by letting u_{R_2} approach infinity (i.e., the outlet is closed) in equation (17). Utilizing this transfer function (17) the time constants for the single variable resistance model (SVR; (18)) and the dual resistance model (DVR; (19)) can be computed.

$$\tau_{SVR} = \frac{C R_i (R_r + u_{R_1})}{R_r + u_{R_1} + R_i} \quad (18)$$

$$\tau_{DVR} = \frac{C R_i (R_r + u_{R_1}) u_{R_2}}{u_{R_2} (R_r + u_{R_1}) + R_i u_{R_2} + R_i (R_r + u_{R_1})} \quad (19)$$

From these time constant definitions, it can be shown that as u_{R_2} approaches infinity (i.e. the outlet is closed) the dual variable resistance time constant (19) converges to the single variable resistance time constant (18). To show the increase in performance of the dual resistance model, the condition of $\tau_{DVR} < \tau_{SVR}$ reduces to a simple inequality (20). Given that each of the values is strictly greater than 0, the inclusion of u_{R_2} always results in a faster system response and remains true for all values of u_{R_1} .

$$R_i (R_r + u_{R_1}) > 0 \quad (20)$$

2.2 Nonlinear Simulation and PI Controller Design

The equation of motion of the nonlinear system (9) was developed into a nonlinear continuous time model using SIMULINK®, which consists of a single feedback loop controlled indicative of a pressure sensor (Figure 2.4). The Linear Actuator Block converts the controller output into a linear actuator displacement. This displacement is regulated by applying constraints to the rate of change (i.e., the velocity of the motor) and the position of the linear actuator ensure that the elastic tubing remains in contact with the actuator. Violation of the latter constraint will lead to negative resistances within the actuator resistance model (12). The velocity of actuator was defined to be consistent with the physical model, at 7mm/s. The Variable Resistor Dynamics Block converts the constrained linear actuator displacement into the variable resistance values which are utilized by the Pressure Dynamics block to implement the equation of motion (9). The static gain

represented in the system converts the standard international units of Pascals (Pa) to the pounds per square inch (psi) represented by the pressure sensor voltage conversion in the physical system. This allows the designed simulated controller to be more directly implemented on the physical hardware. A continuous model was developed rather than a discrete model, representative of all physical systems, because of the 1kHz sampling rate of the pressure sensor. Both models are compared after the implementation of a design controller.

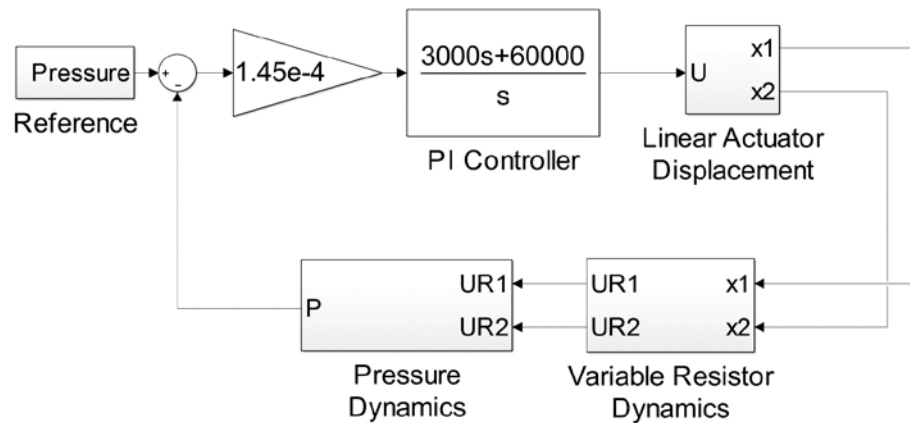


Figure 2.4 Nonlinear Pressure Control Simulink Model

A proportional-integrative (PI) controller was developed for the system, to eliminate the steady-state error for a step input, by minimizing the error between the reference pressure and current pressure value. The PI controller was *ad hoc* tuned to achieved rise time less than 0.3 seconds while maintaining percent overshoot less than 2%, yielding gains of 3000 and 60000 for K_p and K_i , respectively. Other controller tuning approaches (i.e., Ziegler-Nichols) were implemented but could not satisfy the specified design criteria. The control effort is applied, after the completion of the loop, to the linear actuator dynamics to calculate the variable resistances for pressure modulation.

To compare the continuous model to a discrete model, a reference pressure set to decrease from 25.1 kPa to 5.1 kPa at 0.5 s; and a pressure increase from 5.1 kPa to 25.1 kPa at 1 s was generated. The response of the continuous system maintains overshoot less than 1.5%, a settling time less than 0.1 s and zero steady-state error, satisfying the design requirements. The similarity between the discrete and the continuous responses (Figure 2.5) can be attributed to the high sampling rate of the pressure sensor in the discrete time model, 1 kHz, allowing for the reconstruction of the continuous time model.

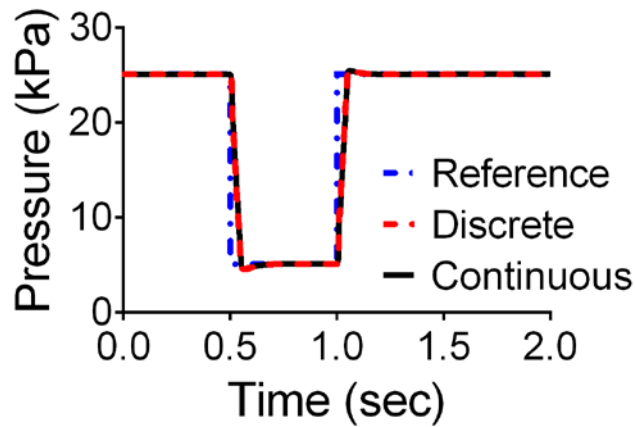


Figure 2.5 Discrete versus Continuous Simulation

The implementation of the designed PI controller on the physical system had to be modified to achieve desired performance due to the higher complexity of the physical system dynamics not represented in the modeling. This complexity includes the differences between the approximated tube resistance and true resistance, the incorporation of tubing elasticity and dilatibility, and noise and/or accuracy error associated with the pressure sensor.

2.3 Experimental System Performance

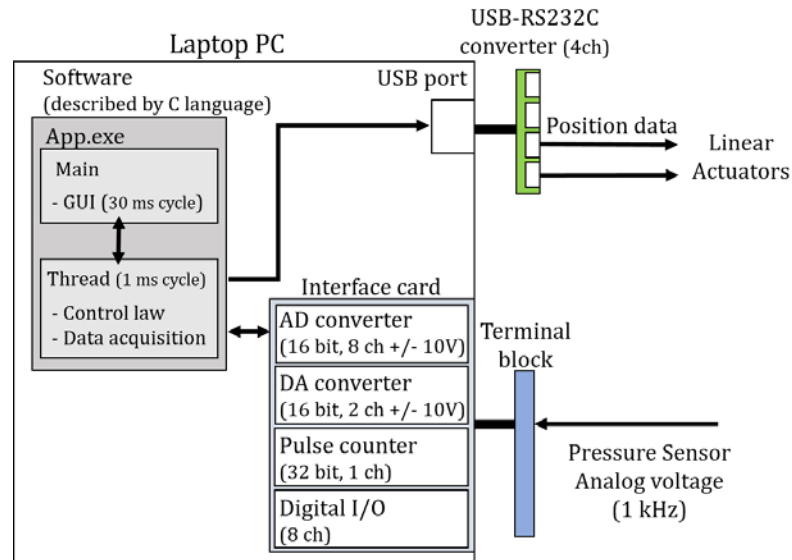


Figure 2.6 Computer Schematic of Pressure Control System

The system was designed with commercially available electronic components:

- Linear actuator, LAC10A-T4-MC04 (Zaber Technologies, Inc., Vancouver, BC, Canada);
- Stepper Motor Controller, A-MCA-KT05 (Zaber Technologies, Inc., Vancouver, BC, Canada);
- 16-bit AD/DA converter CardBus CSI-360116 (Interface Amita Solutions, Inc., Campbell, CA);
- pressure sensors (ASDX series, Honeywell International Inc., NJ);
- USB-COM232-Plus4 (Future Technology Devices International Ltd, United Kingdom)

These components were connected to a laptop computer via a CardBus port, allowing for real-time monitoring of inlet pressure. The control software coded by C language was developed and implemented to the laptop computer. The software was composed of two

different timer threads; the one for a designed PI controller (sensing and control thread) with 1 ms cycle and the other with 30 ms cycle GUI thread for data drawing and interactive parameter tuning (Figure 2.6). A 60Hz filter was implemented in the coding architecture to reduce electrical noise associated with the pressure sensor, increasing overall accuracy.

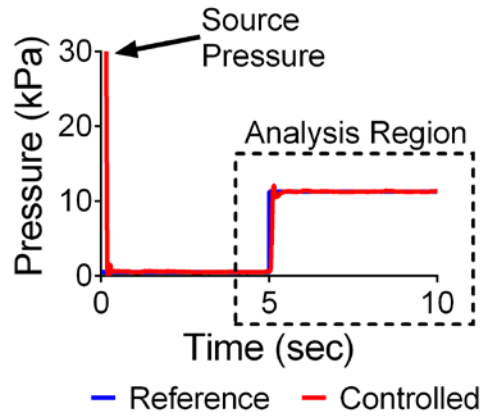


Figure 2.7 Experimental Region of Interest

To evaluate the performance of the controlled system, the responses to both step and sinusoidal inputs were experimentally evaluated at varying degrees of pressure drops and varying frequencies, respectively, to determine the extent of performance. In these examinations, the response was analyzed from the initiation of reference signal, neglecting the initialization of the linear actuators (i.e., both fully pinched tubes; Figure 2.7).

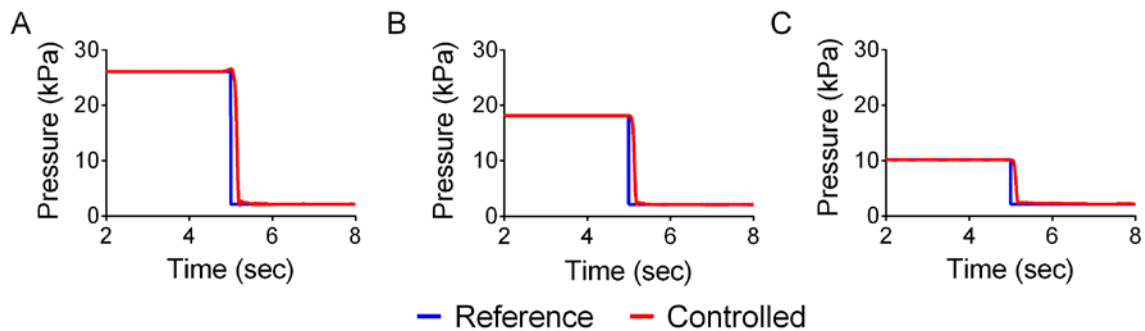


Figure 2.8 Experimental Evaluation of Pressure Drops

Step responses of pressure drops showed settling times less than 0.3 seconds with zero steady-state error (Figure 2.8), where pressure drops of (A) 24, (B) 16, and (C) 8kPa are examined. The speed of the decrease is a function of the tube diameter of the reservoir, a direct correlation to the fluidic drainage. By allowing a larger diameter tubing, more fluidic drainage can occur leading to sharper decrease in pressure. Although a maximum pressure drop of 24kPa was demonstrated, by increasing reservoir tube diameter and applying a well-tuned controller, comparable results can be obtained for larger pressure ranges. A consideration of a larger reservoir is the linear actuator velocity, effecting the volumetric rate of change and pressure modulation.

The profile of the experimental results matches the simulated results (Figure 2.5); however, the settling time of the simulated results remains faster, at less than 0.1 seconds. This discrepancy between experimentation and simulations can be a function of the unmodeled nonlinearities of the physical system and the change of fluidic inertia. The fluctuation in the steady-state values in these step responses is attributed to factors including external disturbances (e.g. air bubbles in the tubing); rippling of tubing due to high elasticity; and linear actuator perturbations. In addition, the pressure sensor has a 12-bit resolution that may restrict the measurable accuracy. These in combination are attributed to the absolute error at steady-state.

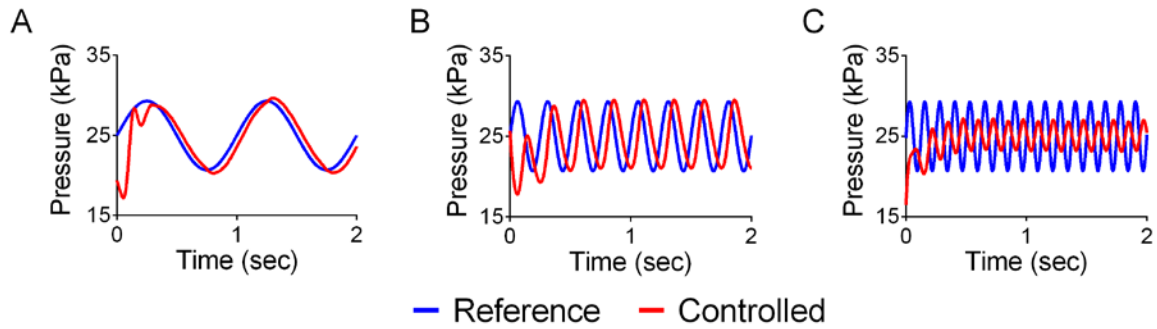


Figure 2.9 Experimental Evaluation of Sinusoidal Pressure Curves

Sinusoidal responses of the pressure control system were observed at (A) 1, (B) 4 and (C) 8 Hz (Figure 2.9). It was observed that as the frequency increases (≥ 8 Hz), limited performance in reference following occurs (i.e., a phase lag and/or a lowered amplitude). Each response can be shown, through the Fast Fourier transform, to match the reference sinusoidal frequency at steady-state. There is a decrease in amplitude, beyond 6 Hz, which can be partially attenuated by increasing the proportional gain; however, remains limited at higher frequencies (>8 Hz). This limitation results from the limited speed at which the linear actuators can change the resistance and transient response of the fluid to a change in pressure differential. Asymmetric sinusoidal and beat signals can be performed with matching amplitude if the maximum frequency remains below 6Hz. The phase lag of the system is attributed to the controller architecture developed. By using a simple PI controller for the system, the error of an oscillating signal cannot be driven to zero. To overcome this limitation, implementation of a zero-phase error tracking control (ZPETC) approaches [121] or more simply by measuring the phase lag, the input signal can be delayed appropriately through command shaping to eliminate the phase lag.

2.3.1 Pressure System Comparison

A previously developed variable resistance-variable reservoir model for the control of the inlet pressure of the microfluidic device [106] was found to contain a mechanical constraint, limiting performance of the system.. The variable reservoir provided an alternative fluidic drainage path for rapid decreases in pressure. To observe differences in performance between the dual resistance model and variable resistance-variable reservoir model, the mechanically linked operation for adjusting the variable resistor and variable reservoir was replaced with the two independent linear actuators. Consistent with the dual resistance model, an increase in pressure is facilitated by a decrease the variable resistance, and a compression of the variable reservoir. This compression in turn contributed to an increase in pressure, resulting in an overestimated overshoot of the controlled pressure. Similarly, when the pressure is decreased an undershoot was obtained. Due to this mechanical constraint of the variable resistance-variable reservoir model, a fluctuation developed (Figure 1.2) within 2 min.

To minimize this fluctuation, the variable resistance-variable reservoir model maintains the pressure by either decreasing resistance to the pressure source or by decreasing the volume of the variable reservoir. Particularly, the time derivative of volumetric change in the variable reservoir was observed as the primary contributor for high-speed pressure regulation. Once the reservoir is fully compressed by the linear actuator, the pressure can no longer be increased. This causes the pressure to decay until the system responds by decreasing the variable resistance, causing a sharp increase in pressure. This pattern is repeated until the system stabilizes within a percent error of the

desired reference signal. Here a PI controller was tuned to achieve an error at stabilization within 2.5%, with a root-mean square of the error of 1.361.

By replacing the variable reservoir with a constant outlet, controlled by u_{R_2} , the dual resistance model eliminates the pressure modulation facilitated by the fluidic drainage mechanism. This reduces the overshoot and undershoot observed in the variable resistance-variable reservoir model and eliminates fluctuation during long-term experimentation (Figure 2.10). By examining the absolute steady-state error, an overall reduction of error below 0.5%, with a root-mean square of the error of 0.030 is observed. The oscillatory behavior observed in the variable reservoir model within two minutes does not arise in the dual resistance model, even after 3 hours of operation. The use of a second variable resistance has consideration with respect to the waste of precursor solution. Because the system is open, the fluid drains out of the system into a collection reservoir, providing reusable material. For long-term experimentation, control of the waste production, related to the controller design, is an important constraint. Within the experiments presented here, the waste was negligible with the controller designed.

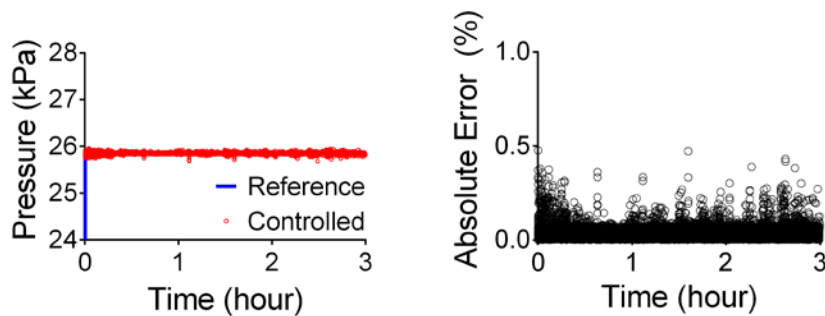


Figure 2.10 Long-Term Pressure System Response

2.4 Conclusions

A long-term, high-speed, and high precision (less than 0.5% steady-state error) system was developed control of microfluidic pressure using the advanced pressure modulation mechanism (the dual resistance model). The nonlinear models were simulated to validate the use of a 1 kHz sampling rate with no signal loss. A continuous time model simulation was performed to show the performance of a linear controller for the nonlinear model. A tuned PI controller was developed, enabling the physical system to have a step response reaching the steady-state within 0.3 s within 0.5% steady-state error. Using the dual resistance model, the steady-state fluctuations that were caused by the previous variable resistance-variable reservoir system [106] were eliminated. This high-precision, high-speed control for long-term experimentation in microfluidic systems can be applied to controlled manufacturing of nanomaterials, which remains a current challenge of syringe-pump based systems. The dual resistance model system can be utilized in a variety of areas including biological instrumentation [47, 122], organ on a chip [123], chemical gradient manipulation (e.g. controlled drug delivery over a tissue) [124], and chemical synthesis (e.g. nanoparticle synthesis) [25, 125]. This work explores the integration of the pressure control system with NP synthesis and large-scale manufacturing to maintain quality control to be addressed in Chapter 3.

Chapter 3 Parallelized Microfluidics for Robust Nanomanufacturing

In this chapter, a parallelized array of microfluidic devices is developed through the process of optimizing the single-reactor synthesis, determining critical parameters for synthesis, and developing models to predict mixing efficiencies of precursor solutions. From the modeling, the parallelized array is refined and optimized to ensure reaction consistency. The device is prototyped with PDMS and further refined prior to final device fabrication. With the feedback pressure control system developed in Chapter 2, the parallelized microvortex array (PMA) is coupled with control theory for robust nanomanufacturing. Lipid-polymer nanoparticles (LPNPs), engineered high-density lipoproteins (eHNP), liposomes (LNPs), and polymeric NPs (PNPs) are explored on the swirling microvortex reactor (SMR) for large-scale manufacturing validation. The process developed within this chapter can further be extrapolated to other microfluidic platforms by following the process described here.

3.1 Swirling Microvortex Reactor

To develop a large-scale parallelized array, the individual SMR needs to be developed and optimized by assessing the critical parameters to NP synthesis. The SMR was initially developed as the single-reactor unit by modeling and tuning the reactor mixing efficiency, a predictive measure of reaction conditions empirically linked to NP size uniformity. Computational fluid dynamics (CFD) simulations to achieve a 90% or higher mixing efficiency with varied SMR diameters (Figure 3.1). The mixing efficiency is a linear scaling of the mass fraction of precursor solutions (Figure 3.2), weighting a 50:50 mass

fraction as the ideal mixing of the precursors, given by equation (21). Using the mixing efficiency metric allows for comparison of not just individual SMR reactor designs but will be used to assess the PMA reactor consistency and comparison to the SMR.

$$Mix_{eff} = \begin{cases} 2M_{fract}, & M_{fract} < 0.5 \\ 2(1 - M_{fract}), & M_{fract} \geq 0.5 \end{cases} \quad (21)$$

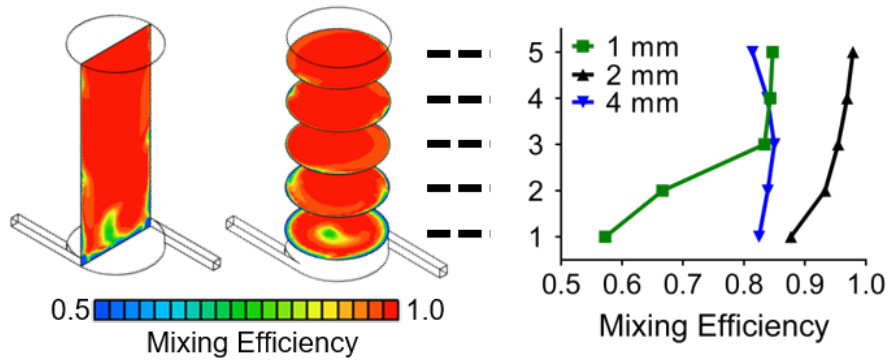


Figure 3.1 SMR Development

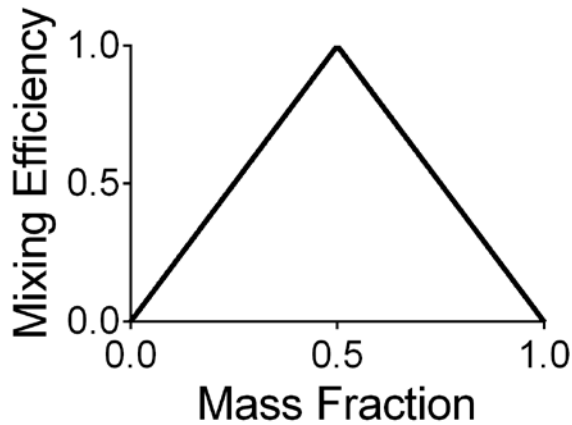


Figure 3.2 Mixing Efficiency Standard

The mixing efficiency of SMRs with diameters of 1mm, 2mm, and 4mm have characteristic mixing times (4ms, 16ms, and 64ms, respectively) less than the residence time (20ms, 40ms, and 80ms, respectively) of the reactor when the height is held constant

at 5mm. The larger the reactor, the larger the characteristic mixing (τ_{mix}) and residence times (τ_{res}) become. Specifically, the characteristic mixing time remains lower than the residence time while the hydraulic diameter, the SMR outlet diameter, is less than the height of the reactor. Larger reactors have greater LPNP production rate, due to higher flow rate, but decrease the number of reactors per unit area; conversely, smaller reactors decrease LPNP production and increase the multiplicity of reactors per unit area. Governed by equations (22)-(23), where D_h represents the hydraulic diameter of the reactor, v represents the fluid velocity, V represents the total reaction volume, and Q represents the total flow rate.

$$\tau_{mix} = \frac{D_h}{v} \quad (22)$$

$$\tau_{res} = \frac{V}{Q} \quad (23)$$

With the tuned SMR, highly reproducible LPNPs are continuously produced with high size uniformity at a rate of 3g/h (Figure 3.3), based on inlet flow rates and concentrations with 100% yield. LPNPs combine the unique strengths of LNPs and PNPs while overcoming their limitations in terms of drug encapsulation efficiency and storage stability [63, 64], respectively. The simulations were experimentally validated by synthesizing LPNPs in the SMRs with various diameters (1mm, 2mm, and 4mm) at a constant Re of 250 (Figure 3.4A), a transitional boundary above which swirling vortex flow patterns become chaotic.

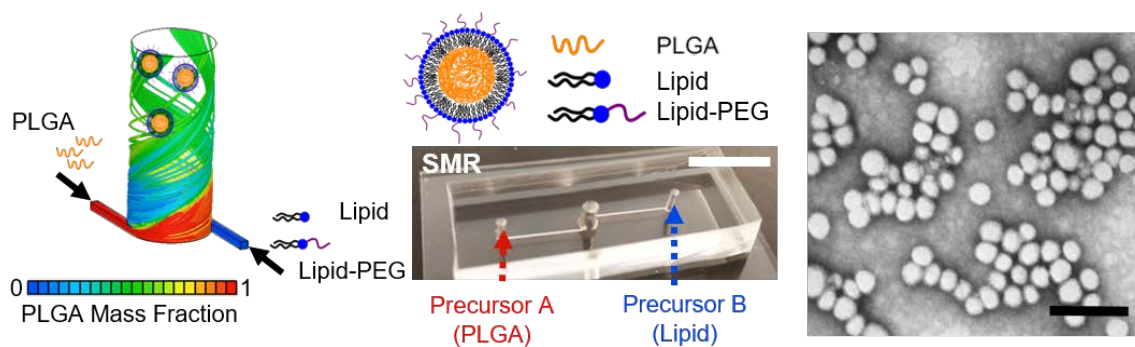


Figure 3.3 SMR LPNP Production Schematic

The 2mm diameter, where computationally, the highest mixing efficiency (0.92, volumetric average in a SMR) was obtained; demonstrated the narrowest LPNP size distribution (Figure 3.4A) in the experimental synthesis validation. The size distribution and NP quality were demonstrated to have fine control with respect to the precursor composition (Figure 3.4B) and the ability to control the size simply by varying flow rates (i.e., Reynolds numbers; Re) without changing the precursor composition (Figure 3.4C). Increasing the Re into the chaotic regime above 250 doesn't cause a further decrease in the NP size or quality, indicating a physiological limit of LPNP on the SMR platform. For large scale parallelization, the minimization of precursor composition variation is more critical than minimization of Re variations because of the high operating Re of 250.

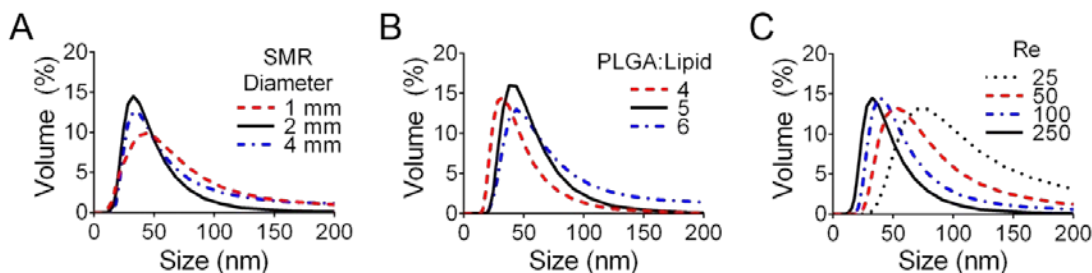


Figure 3.4 SMR Experimental Nanoparticle Synthesis Validation

3.1.1 Pressure Control Integration and Analysis

To produce NPs with high reproducibility, the SMR was integrated with the custom high-precision, feedback pressure control system detailed in Chapter 2. To calculate the synthesis conditions, first the SMR was decomposed into equivalent resistances and constructed a fluidic circuit analog of the coupled system with both inlets (Figure 3.5). Coupled with the equation for Re [79, 126], the SMR inlet pressure is given as below (24).

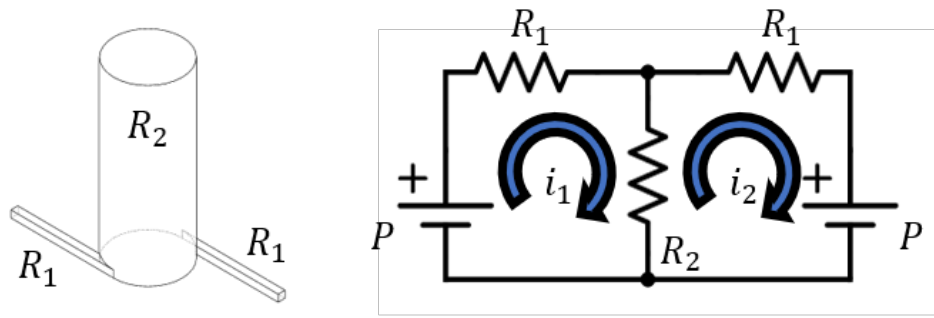


Figure 3.5 Electrical Decomposition of SMR

$$P = \frac{[R_1 + 2R_2]\mu A}{2\rho D_H} \cdot Re \quad (24)$$

$$R_c = \frac{8\mu L}{\pi r^4} \quad (25)$$

$$R_s = \frac{12\mu L}{wh^3 \left(1 - 0.63 \frac{h}{w}\right)} \quad (26)$$

where μ represents the dynamic viscosity, A represents the cross-sectional area of the SMR, ρ represents the fluid density, D_H represents the hydraulic diameter, and Re represents the Reynolds number. The definitions of the R_1 and R_2 are given by the respective square (26) and circular (25) resistances. This equation (24) is used to calculate the pressure range corresponding to the Re designed in this study (Figure 3.6A). As previously discussed, the control system demonstrated the performance with less than a 0.3

second settling time is maintained across the various Re (Figure 3.6B). The performance of the pressure control system (PC) was compared with a commercially available syringe pump (SP); demonstrating a 50 times faster transient response (Figure 3.6C) and more stable in long-term regulation of a flow rate (Figure 3.6D). Both the transient and steady-state response of the PC demonstrate more robustness than the SP, impacting the flow rates for NP synthesis and, ultimately, NP quality.

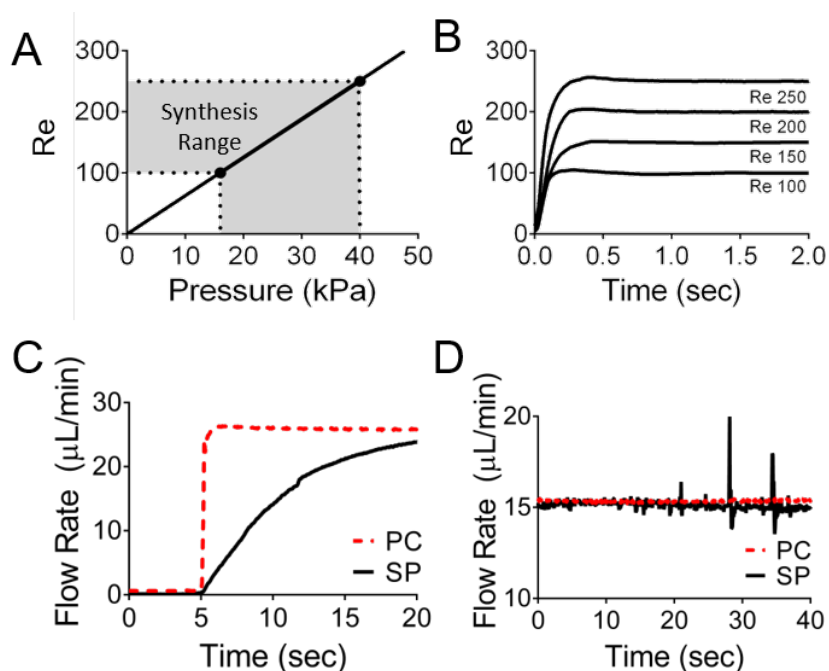


Figure 3.6 SMR Feedback Controller Performance

With this superior performance of the high-precision control system, the size uniformity of NPs synthesized on the SMR were assessed by comparing the size distributions and the polydispersity index (PDI), a measure of the homogeneity of the size distributions. LPNPs produced on the SMR using the developed feedback pressure control system demonstrated narrower size distributions than those using a syringe pump for steady-state (long-term) (Figure 3.7A and B) and transient (short-term) performance

(Figure 3.7C and D). The transient response includes the prefilled channel where mixing conditions are not ideal; leading to higher PDI, especially for systems exhibiting long transient flow responses (e.g., syringe pumps). The steady-state response is taken after the ideal mixing conditions are achieved

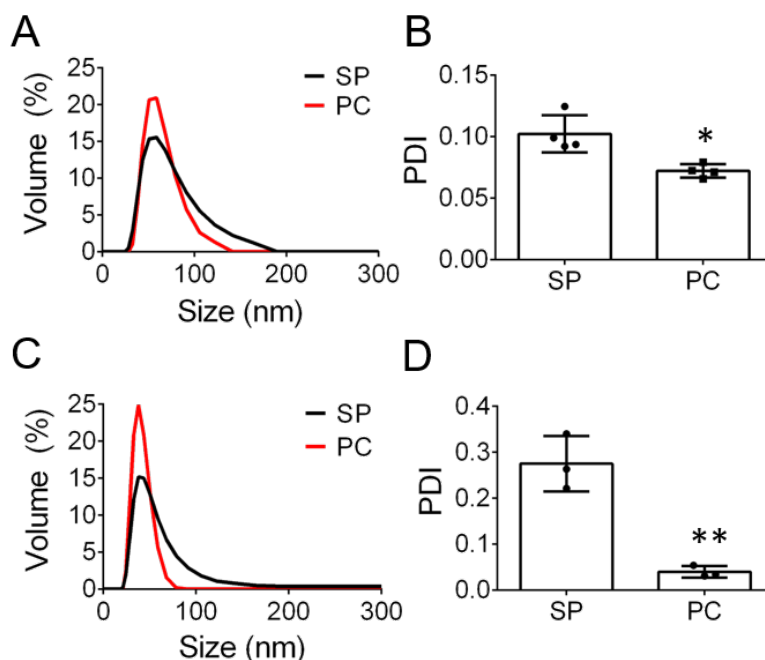


Figure 3.7 Steady-state/Transient Nanoparticle Synthesis Comparison

The difference in the NP distributions and PDI values from the steady-state response is because feedback pressure control system rejects external disturbances and minimizes the variation in the inlet pressure of the SMR (Figure 3.7A and B). This disturbance rejection preserves the Reynolds number and precursor composition, which are two critical factors that affect NP physicochemical properties. The difference in the NP distributions from the transient response is because it takes longer (settling time upwards of minutes) [92, 93] for the syringe pump to reach steady-state values than for the feedback pressure control system (less than 0.3 second settling time response) (Figure 3.7C and D).

3.1.2 Nanoparticle Versatility

Although LPNPs have a broad range of applications, research for engineered high-density lipoproteins (eHNPs), liposomes (LNPs) and polymeric NPs (PNPs) remains active. Each of these particle types have been developed into nanotherapeutics for a treatment of an enormous range of diseases. Repeatable synthesis and narrow size distributions are essential to such applications. Therefore, to explore the versatility of the SMR, each of these nanoparticle formulations were examined.

High-density lipoprotein (HDL) is a rapidly expanding area of research [4, 127-130] because of ability to incorporate therapeutics and cross the blood-brain barrier. This synthetic HDL are referred to as engineered high-density lipoprotein (eHNP). Composed of apolipoprotein A1 band around a lipid disk, nascent eHNP is commonly responsible for the removal of cholesterol from the body by removing cholesterol, promoting overall health. Both computationally [131] and experimentally [130], discoidal eHNP was found to be around 10 nm is size. Discoidal eHNP synthesized on the SMR (Figure 3.8) was consistent with current research. Further study needs to include the incorporation of cholesterol, changing the morphology to spherical particles, and therapeutic agents. Additionally, there are several types of apolipoprotein that can modify the chemistry and reactivity of eHNP for new nanotherapeutics.

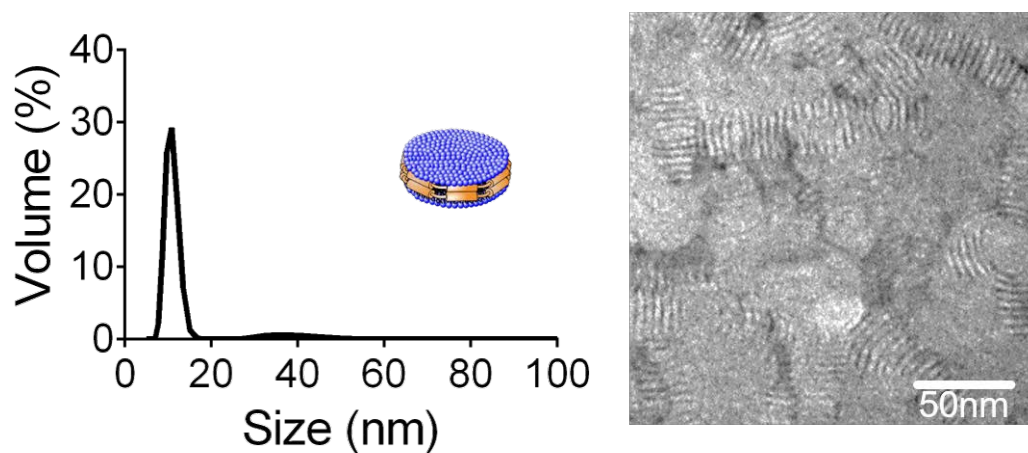


Figure 3.8 SMR Synthesized eHNP

Polymeric nanoparticles (PNPs; Figure 3.9A) have been used and developed because of their high drug loading capacity and ease of synthesis. Requiring the reaction of PEGylated PLGA with water, PNPs have been commonly synthesized with diffusion-based microfluidics [19, 83] with more recent approaches demonstrating turbulent impinging mixing [32] with an average particle size of approximately 33 nm. Synthesizing PNPs on the SMR at various concentrations (Figure 3.9B) yields interesting results, whereas the concentration or the precursor solution is increased the size of the particle decreases. This can potentially be the result of the increase in concentration decreasing the distance between molecules, allowing for more rapid synthesis of stable particles. This is coupled with the particle-particle interactions that may prohibit the formation of larger particles. Each of the cases additionally has a proceeding tail of large PNPs due to the reaction. This may be related to the use of a 50:50 ratio of water and acetonitrile (organic solvent for PLGA-PEG). The previous diffusive and turbulent approaches only used a 5% acetonitrile concentration in the finalized product [19, 83]. To examine the effect of the acetonitrile (ACN) concentration, the 15 mg/mL case was examined with the 50% ACN of

normal synthesis (i.e., Re 250 with equal precursor flow conditions), 25% ACN by prefilling the collection vial with water with normal synthesis, and 10% ACN by creating asymmetric flow conditions (Figure 3.9C). The hypothesis of the increase in the ACN is that ACN can potentially cause particles to disassociate leading the larger aggregations. The observation shows that when smaller percentages of ACN are used there is a decrease in the tail size. Interestingly, the water prefilled approach lead to the smallest decrease in the PNP tail and peak size (19nm). The reaction needs to be further refined based on these results to minimize the trailing edge of the size distribution, an indication of a polydisperse mixture.

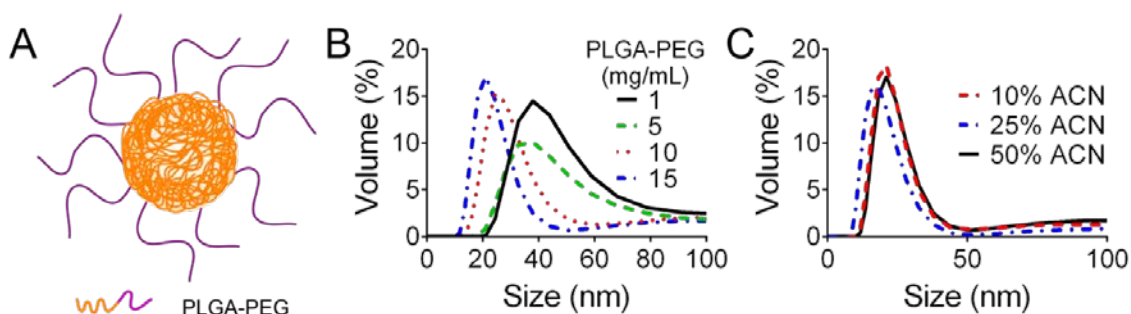


Figure 3.9 SMR Synthesized PNP

Lastly, liposomes (LNP; Figure 3.10A) have been developed as nanotherapeutics because of their biocompatibility [54, 55, 132], easily tunable surface chemistry, and natural occurrence in vivo. Comprised of a lipid-bilayer, LNPs can be formed by reaction a solution of lipids, in ethanol, and a solution of water. The complexity of the reaction is that there is a potential biproduct of micelle formation, a single layer particle with a hydrophobic core. As the concentration of the lipid (DPPC) is reduced size of the particle is reduced (Figure 3.10B). The large size of the particles indicates the aggregation of lipids/particles at higher concentrations, forming macroparticles. The 0.25 mg/mL

concentration yields a small size of 100 nm particles; however, the mixture is very polydisperse. The refinement is multifaceted, as a function of both the initial lipid concentration and the final synthesized ethanol concentration. Since the reaction is dependent on solvent inversion, having a 50% solution of ethanol, like the PNP case, can result in the dissolution of formed LNPs and possibly lead to aggregation during the filtration process. To examine the effect of the ethanol (EtOH) concentration, the 1 mg/mL case was examined with the 50% EtOH of normal synthesis (i.e., Re 250 with equal precursor flow conditions), 25% EtOH by prefilling the collection vial with water with normal synthesis, and 10% EtOH by creating asymmetric flow conditions (Figure 3.10C). The results demonstrate that as the percent solvent is decreased, the size of the LNP is decreased as well. The lowest case (10% EtOH) is consistent with previously reported literature [133]. The lipid solution does not contain pegylated lipid, as in the synthesized LPNP, which can help to stabilize the particle and potentially prevent this aggregation. The optimization of the reaction needs to be looked at from multiple viewpoints to discern process by which LNPs form on the SMR.

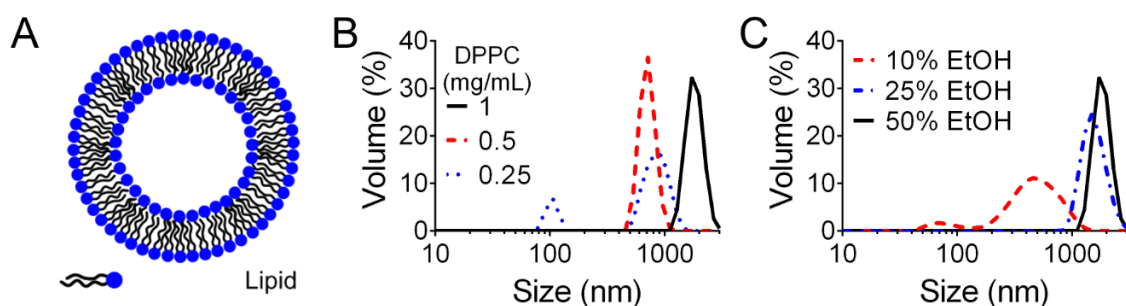


Figure 3.10 SMR Synthesized LNP

Each of these alternative NP formations needs to be further refined and modified to be utilized as a nanotherapeutic, but with the distributions and discussion, the potential of

these platforms on the SMR device has been shown. The single component synthesis with PNPs and LNPs needs to further be explored as it is no longer dependent on a ratio of precursors but rather the mixing conditions, related to the Re , the solvent concentration, and precursor composition. The optimization of these syntheses will need to be further studied to better understand and refine the NPs. In addition to refining the synthesis of the individual formulations, the incorporation of drugs (e.g., doxorubicin) needs to be evaluated on the SMR for nanotherapeutic development. The demonstration of the NP formulations on the single-reactor can be extended through the parallelization of the SMR for nanomanufacturing.

3.2 Parallelized Microvortex Array

To develop the large scale parallelized microvortex array (PMA) of SMRs, it is critical to maintain reaction consistency to ensure a uniform and narrow size distribution across all SMRs. In the development of the SMR, both the Re and the mass fraction of the precursor solutions were found to be the two parameters affecting the size distribution (Figure 3.4). From these two variables, the minimization of the precursor composition is most critical to reactor consistency because small variations resulted in a size shift up to 10nm (Figure 3.4B). The variation of the Re is less critical for parallelization as the system operates at the physiological limit (Re of 250) where small variations minimally affect the size distributions (Figure 3.4C). For the modeling and development of the PMA, both variables will be minimized to achieve high-precision nanomanufacturing.

3.2.1 Fluidic Circuit Analog Modeling

To develop the PMA, a network of microfluidic channels needs to be constructed connecting a multiplicity of SMR with common precursor inlets and a common outlet

(Figure 3.11A). The dimensions of the channels need to be determined based on equations (23-25), to minimize the pressure differentials between each SMR based on channel impedances. Similar to determining the pressure differential of the SMR integrated with the PC, the microfluidic network is decomposed into an equivalent electrical system.

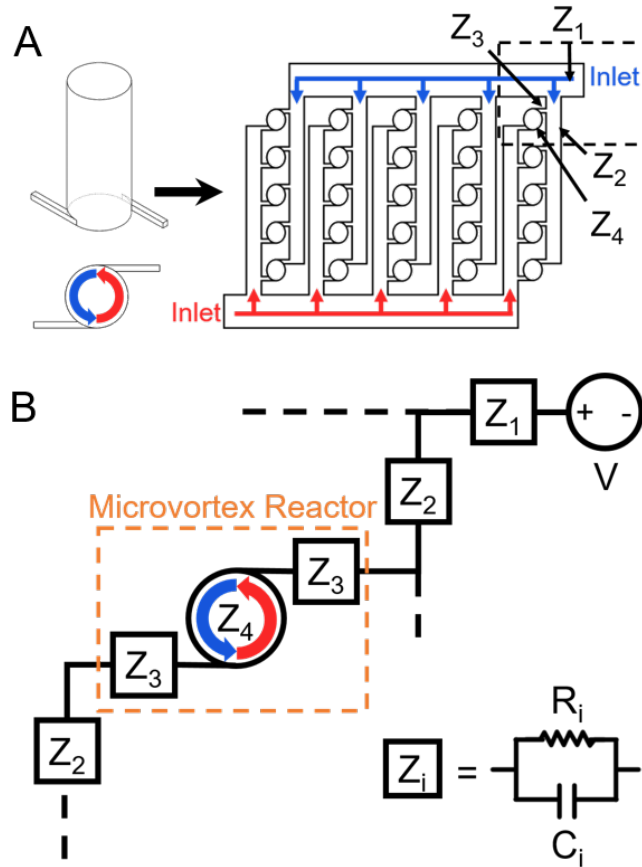


Figure 3.11 PMA Fluidic Circuit Analog Decomposition

A fluidic circuit analog [88] to optimize the PMA inlet fluidic impedances (Z_1 and Z_2) given the SMR inlet impedances (Z_3 and Z_4) (Figure 3.11B) was developed. Each fluidic impedance consists of the fluidic resistance, R , and capacitance, C . To minimize pressure variations at the inlet of each SMR in the PMA, the microfluidic channels networking the SMRs should lead to an identical pressure drop between the pressure source and the inlet

of each SMR. This methodology is accomplished by equating the Hagan-Poiseuille equation for fluidic systems with Ohm's Law for electrical circuits, assuming an incompressible Newtonian fluid in laminar flow. Within the microfluidic channel hierarchy (Figure 3.11B), the $Z_2:Z_3$ ratio was found to be a key design parameter to be tuned to minimize pressure variations at the inlet of each SMR in the PMA. The ratio is indicative of a smaller Z_2 resistance represented by a larger channel. The lower the resistance leads to a smaller pressure drop between each SMR, governed by the Hagan-Poiseuille equation. To determine a desired $Z_2:Z_3$ ratio, the flow rate ratio (27) between the inlets of the first and Nth SMR within a PMA column and found that an increase in the array size (i.e., the number of the tuned SMR in a PMA) requires a decrease in $Z_2:Z_3$ ratio to maintain the same flow rate ratio. The flow rate ratio assumes that Z_4 is much less than either Z_2 or Z_3 , which is the case for this system. Ideally, the flow rate ration between the first and Nth reactor should be 1. More importantly, the flow rate ratio in a larger array size is more sensitive to the variations in the $Z_2:Z_3$ impedance ratio, requiring a higher accuracy for fabrication in a larger PMA, generally increasing production costs (Figure 3.12). In the current platform of 5x5 array, a flow rate ratio (0.92) was utilized resulting in a $Z_2:Z_3$ ratio (0.021). This mathematical approach allows for the extension to a NxN array, allowing for researchers to tune the multiplicity of scaling for various applications.

$$Flow\ Rate\ Ratio = \frac{q_N}{q_1} = \left(\frac{Z_2}{Z_3} (N - 1) + 1 \right)^{-1} \quad (27)$$

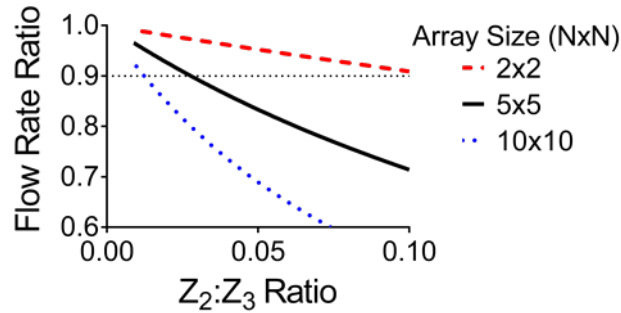


Figure 3.12 Array Size Sensitivity on Design Criteria

The calculation of the flow rate ratio (27), allows for the optimization of the $Z_2:Z_3$ ratio through iterative coding process. By setting the height of the array to 200 μ m, the height of the SMR inlets, defining the parameters of Z_1 , and the width of Z_2 (3.5mm), the coding algorithm can find the design criteria for the system to achieve a desired flow rate ratio. Additionally, the overall size of the device (Figure 3.13), a critical constraint for manufacturing, can be approximated from the rectangular channel design, assumed in the electrical model (Figure 3.14A).

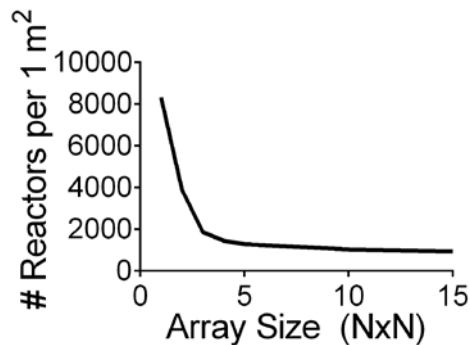


Figure 3.13 Reactors per Array Size

The area analysis demonstrates that the system reaches a horizontal asymptote, where the reactors per 1m² achieves approximately 1000 reactors. The multiplicity of the PMA design, can increase the reactors of the system, reducing overall number of reactors per

area, or place a large number of small NxN reactors in parallel, requiring the additional control system for proper synthesis. Coupled with the increased fabrication costs of higher dimensional arrays, a cost analysis of the overall system can be assessed to optimize the design for manufacturers.

3.2.2 Design Optimization

The use of a fluidic circuit analog provides the general dimensions; however, the rigid nature of the design does not incorporate the complexity of fluid dynamics, in particular the Navier-Stokes equations. To further analyze and optimize the PMA design, CFD simulations were used to further tune the electrical PMA model by minimizing local flow variations across the initial (Figure 3.14A) and tuned fluidic (Figure 3.14B) models, finalizing the PMA design with less than 1% precursor composition variation and less than 4% Re variation (Figure 3.14C). The optimization of the PMA design increased the pressure differential required for ideal synthesis, caused by an increase in the resistance, and created a more uniform pressure distribution for each inlet. Due to the increase in the resistance of the PMA, the required inlet pressure for the device is increased, requiring a modification to the feedback pressure control system with a larger range sensor and controller tuning.

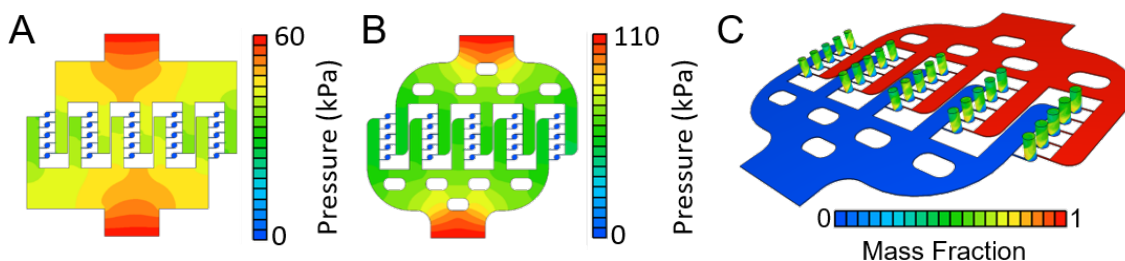


Figure 3.14 PMA Computational Fluid Dynamic Simulations

This refinement of the PMA model simulated with the ideal PLGA-to-lipid weight ratio of 5 and the ideal Re of 250 decreased the variation of the precursor composition at the inlet of each SMR in the PMA by 79.4% (Figure 3.15A) and improved the mixing consistency across the SMRs by 1.5% (Figure 3.15B) and across the height of the SMR (Figure 3.15C). While the average mixing efficiency in the outlet of the PMA (91%) was lower than that of the tuned SMR (98%) (Figure 3.1), the difference was not significant as a mixing efficiency above 90% showed comparable NP size distribution in the experimental data (Figure 3.4A-C).

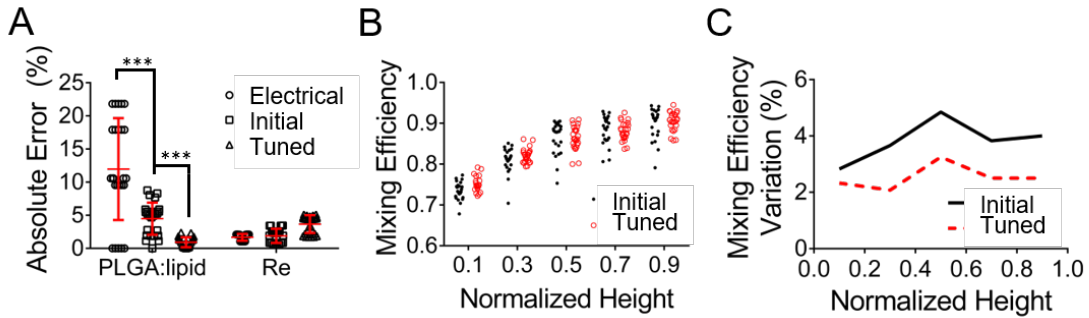


Figure 3.15 PMA Modeling Analysis

3.2.3 Prototyping and Fabrication

To implement the design of the PMA and validate the model, a prototype was initially developed utilizing the common photolithography techniques for microfluidics in combination with machined molds (Figure 3.16), consisting of 3 distinct layers: 1. Parallelized microfluidic array network, 2. Microfluidic reactor pillars, and 3. Collecting reservoir. Initially the prototype was modeled after the electrical fluid analog (Figure 3.14A) where each of the channels are rectangular with a set height of 200 μ m. The initial prototype was found to be inadequate for the device because the large surface area of the

Z₁ channels collapsed and bound to the lower substrate (i.e., layer 2 bounded to layer 1), disrupting the carefully designed channel dimensions and ultimately modifying the fluid dynamics. Additionally, the sharp corners of the device were found to entrap bubbles, disrupting the dynamics of the system.

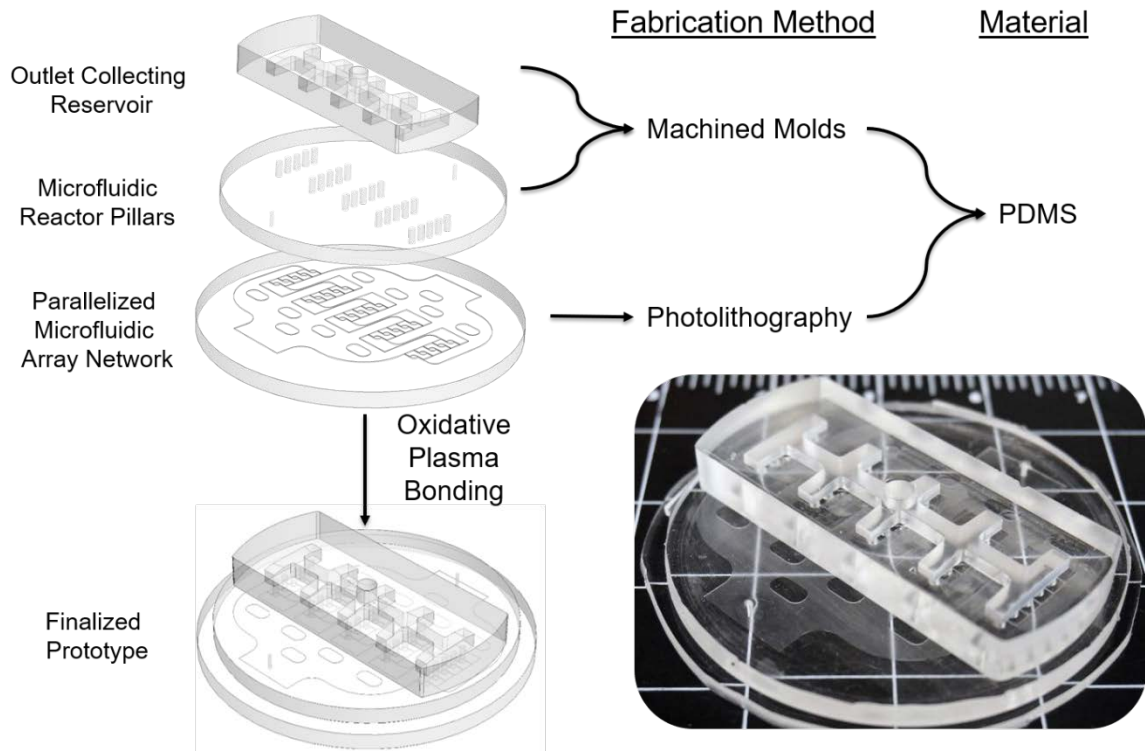


Figure 3.16 Polydimethylsiloxane PMA Prototype Schematic

The material selection for rapid prototyping for microfluidics is generally polydimethylsiloxane (PDMS). Using this material for the with the PMA systems presented numerous issues needing to be addressed for proper functionality. During synthesis, the PDMS experienced large nonlinear deformation under the large pressure differential applied to generate the Re 250 flows. The deformation disrupts the designed microfluidic channels causing large Re and precursor variation across all the channels. This deformation was caused by the low Young's Modulus of a PDMS-PDMS bond [30].

PDMS is incompatible with organic solvents for long durations, and the porosity of the materials allows for material absorption over time. The inlet connection with microfluidics often use compression fitting by sticking either a polyethylene tube or metal needle into a punched PDMS hole. The high pressure required for the use of the system dislodges the tubing, causing a device failure and potentially exposing researcher to hazardous chemicals (e.g., acetonitrile). Each of these issues decreases the longevity and versatility of the design, requiring modification to overcome the limitations.

3.2.4 Robust Nanomanufacturing with Feedback Control

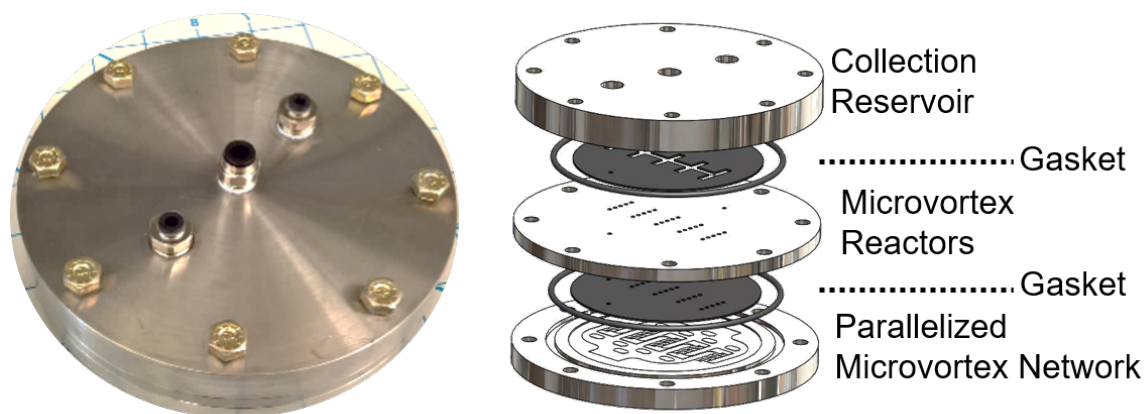


Figure 3.17 Robust PMA Design

Improving the design of the PMA, the PDMS was replaced with a more robust 304 stainless steel construction, overcoming both the material incompatibility and the nonlinear deformation found in the PDMS model. Due to the use of stainless steel, the device could no longer be plasma bonded to eliminate leakages and reactor-reactor contamination. Inserted between each of the layers was two ethylene propylene diene monomer (M-class) rubber (EPDM) gaskets, compatible with organic solvents (e.g., acetonitrile). To prevent leakages of the system, 8 radially spaced bolts were equally compressed with 25lb-in of

torque. Lastly, to prevent failure of the device, through tubing disconnection, high pressure push-to-connect fittings were integrated into the design for both inlets and the outlet. Combining all the modifications, the device is compatible with a variety of solvents, doesn't deform under the required pressure differential, and is easily separable for cleaning surfaces between reactions, if necessary.

To minimize the SMR-to-SMR variation of critical reaction parameters, the inlet flow for each precursor is regulated by the feedback pressure control system (Figure 3.18), discussed in Chapter 2, to mitigate inlet flow variations in the PMA, a factor that amplifies designed parameter variations (i.e., Re and precursor composition).

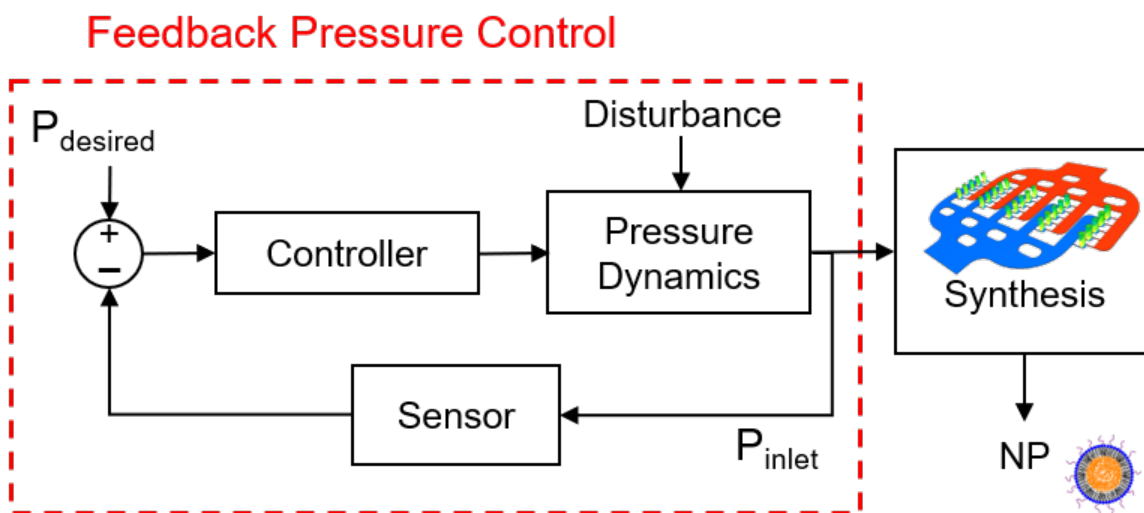


Figure 3.18 Feedback Control PMA Integration

By coupling the PMA with the high-precision, feedback pressure control system to regulate the inlet pressure of the PMA external disturbances are mitigated, and precursor flow fluctuations are reduced. To demonstrate the advantage of coupling the feedback control system, production of LPNPs with and without the control in response to an external disturbance are compared (Figure 3.19). Without the mitigation of flow

fluctuations, generated by external disturbances, the NP size uniformity is substantially reduced. The integration of the PMA with the feedback control provides not only highly reproducible uniform LPNP production for long-term duration but also mitigates external disturbances that would otherwise cause a failure to achieve robust manufacturing.

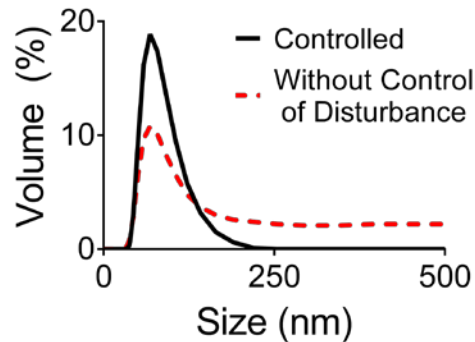


Figure 3.19 Controlled LPNP Synthesis on PMA

Comparing the distribution of the PMA to the single SMR (Figure 3.20), the distributions of both systems are comparable. Compared to bulk mixing process [25, 29], the polydispersity of the PMA distribution remains lower than that of conventional bulk mixing while achieving a continuous synthesis process. Providing a means to accelerate the clinical translation of nanotherapeutics with higher reproducibility, the PMA has a robust design for a broad range of applications with the design of the system allowing for modification.

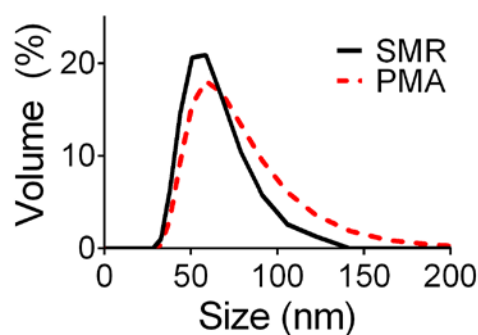


Figure 3.20 LPNP Synthesis Comparison of SMR vs PMA

3.3 Conclusions

A representative example for robust manufacturing (1.8kg/d) of multicomponent NPs through feedback controlled, parallelized microfluidic reactors has been presented. The unique design of a microfluidic reactor was developed into a parallelized array for large-scale production of NPs while maintaining the mixing time scales of the single reactor and the physicochemical properties (e.g. size) of produced NPs. The impedance ratio of a microfluidic channel network linking individual reactors to impedance of individual reactor inlet was found to be a key design parameter to be minimized, ensuring reaction consistency in a parallelized platform. The microfluidic parallelization approach demonstrated that LPNPs could be manufactured without losing the physicochemical properties (i.e., size), and the production process could be within a manufacturing quality with feedback control. The parallelized reactor design can be further extended to a larger array, achieving a greater production rate that addresses the current manufacturing challenges that pharmaceutical and biomedical industries face. The integration of advanced microfluidic technology with control systems engineering may validate a new impactful method for robust NP manufacturing and contribute to efficient development and

optimization of a wide range of multicomponent NPs for therapeutic and diagnostic applications.

Chapter 4 High-Precision Feedback-Controlled Fluidic Sampling

In this chapter, a tunable low-cost high-precision feedback-controlled sampling apparatus to automatically sample specified volumes and times is developed. The design of the rotational feedback controller is first modeled and experimentally validated with settling times less than 0.3 seconds, overshoot less than 2%, and zero steady-state error. The design constraints of the microvolumetric sampler are discussed, including multiplicity and size of sample effect on the controller implementation. After outlining the performance of the device, the microvolumetric sampler device is integrated with an organ-on-a-chip platform [43] to demonstrate the robust high-precision sampling of drug dosages. The analysis of cellular drug/compound loading is extended by computationally assessing the effect of membrane porosity.

4.1 Microvolumetric Sampler Development

To develop the automated microvolumetric sampler device (Figure 4.1) for high precision temporal and volumetric control of biological samples, the rotary motor integrated with the PDMS microvolumetric sampler and syringe pump systems was first designed and fabricated. The approach of the device was to allow researchers to set the desired volume of a sample at discrete time points without the introduction of human variation, a potential source of error or variation across repeated studies. The accuracy of the device will be reliant on the flow control system (i.e., syringe pump or pressure control system) and the precision operation of the sampling device. Because most of the microfluidic field utilizes syringe pumps, the developed feedback pressure control system, described in Chapter 2, was not used.

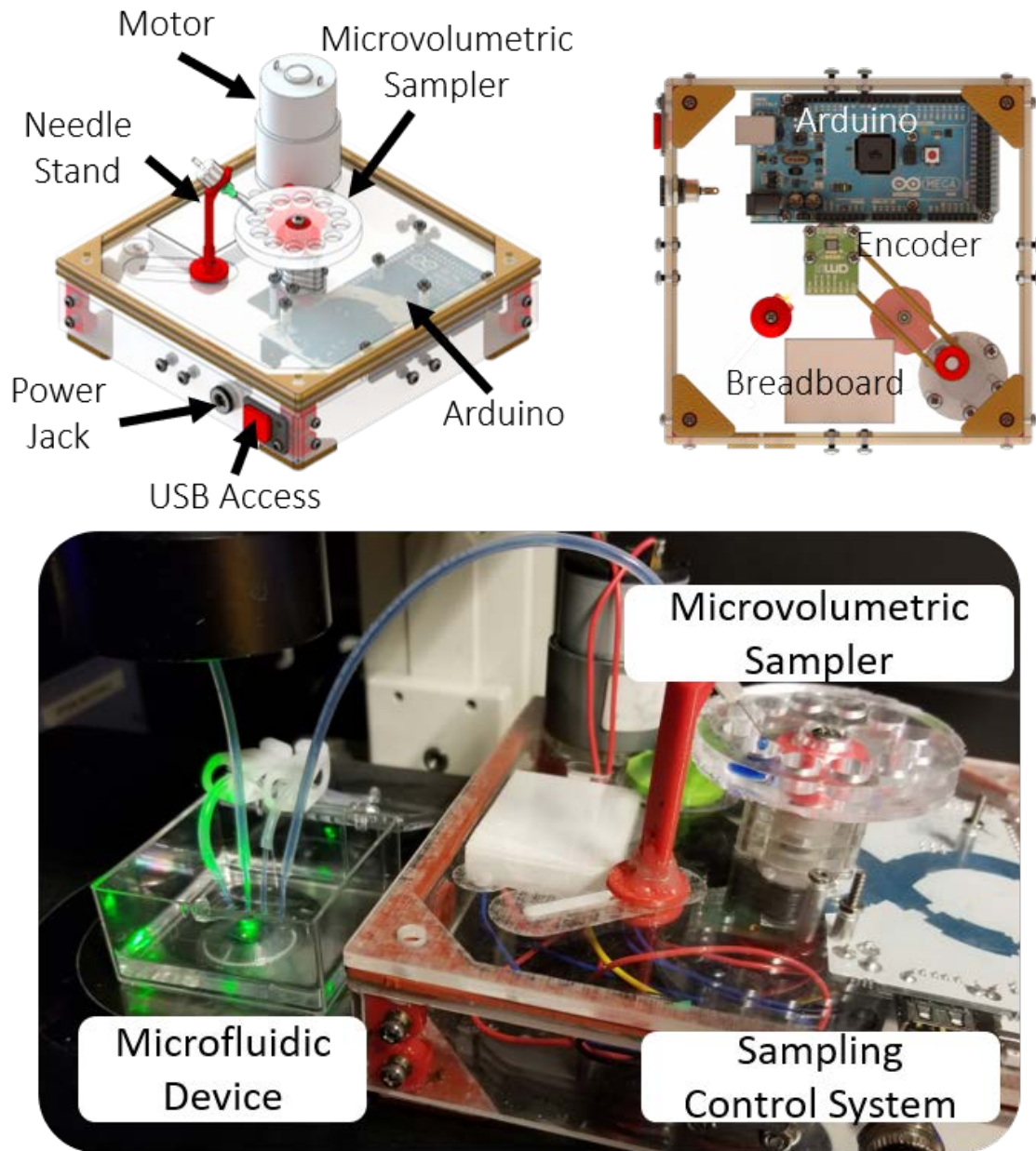


Figure 4.1 Sampling Device Schematic and Integration

In addition to precision sampling, the design allows for researchers to sample biological agents in a microfluidic device, commonly used for organ-on-a-chip [43]. The design of the chip contains an upper and lower channel separated by a porous membrane (Figure 4.2).

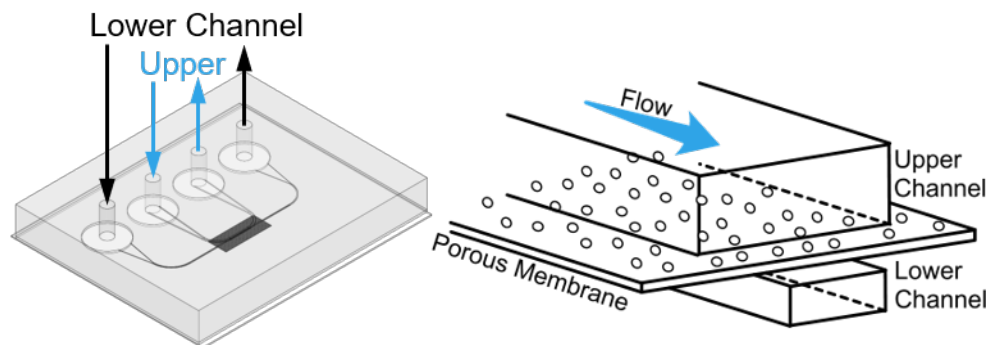


Figure 4.2 Integrated Organ-on-a-chip Schematic

To accurately measure these biological samples, the microvolumetric sampler is automatically rotated at specific intervals based on the desired volume and output flow rate of the system (Figure 4.3). Where the time to fill each well (T_{well}) is dependent on both well volume and desired flow rate (Q_d). The overall apparatus was designed to incorporate microvolumetric samplers with larger sample volumes and/or multiplicity of samples, allowing for broader range of research applications. The basis for the performance of the microvolumetric sampler relies on the precision of the motor to accurately rotate the system while minimizing overshoot and settling time.

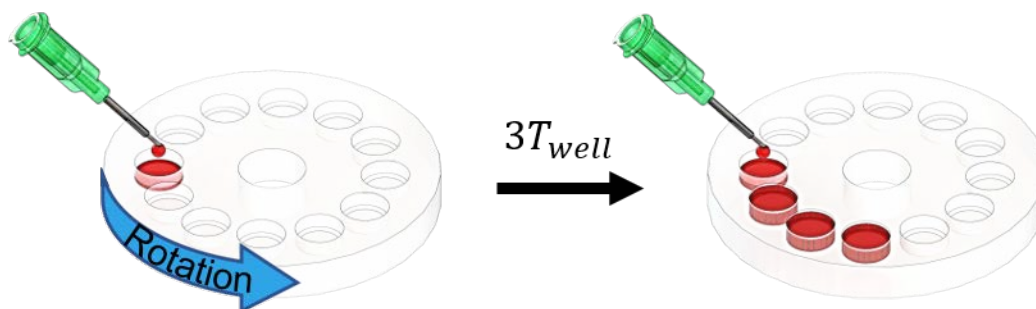
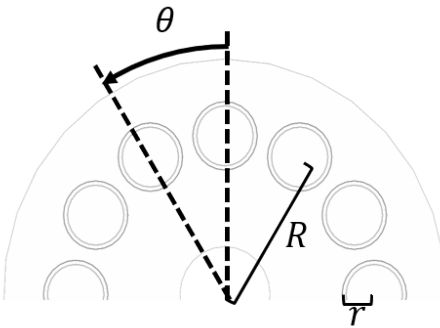


Figure 4.3 Sampling Device Operation Schematic

4.1.1 Controller Development

For the development of the motor dynamics and requirements, the properties of the microvolumetric sampler are first analyzed. The microvolumetric sampler can be expanded to include either larger/smaller wells a larger/smaller multiplicity of wells, generating design constraints by modifying both the sample volume and experimental duration. The maximum allowable angle between wells and the calculation of the time differential (Figure 4.4), based on cylindrical wells, are both used as initialization inputs for the microcontroller for proper functionality. The use of a circular cross-section at the surface of the microvolumetric sampler maximizes the area for sampling. By centering the needle in the center of the circular cross-section, the possibility of either the sample missing the well or the rotation overshooting a well is greatly reduced. Because of the circular cross-section of the well, the design of the well can be modified to account for desired sample volume by either implementing cone or round bottom cylindrical geometry without the need to redesign the controller.



$$\#wells = \left\lfloor \frac{\pi}{\tan^{-1} \frac{r}{R}} \right\rfloor$$

$$\theta = \frac{2\pi}{\#wells} \quad T_{well} = \frac{\pi r^2 h}{Q}$$

Figure 4.4 Microvolumetric sampler Mathematical Constraints

The requirements of the controller were determined to be less than 0.3 setting time, less than 2% overshoot, and zero steady state error. These requirements were chosen to not overshoot a well, leading to potential sample deposit in an undesired well, and to remove compound error, potential overshoot over long experimental duration. The design of the controller is reliant on feedback from the encoder (28) for precision movement (Figure 4.5). The encoder dynamics include unity gain ($K=1$) and a sampling time (T_{samp}) of 250ns, simplifying the overall model dynamics of the system.

$$H(s) = \frac{K}{T_{samp}s + 1} \cong 1 \quad (28)$$

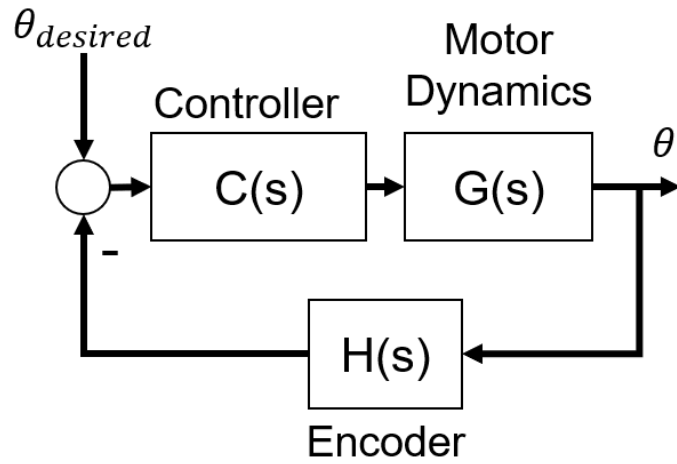


Figure 4.5 Motor Control Block Diagram

To develop an appropriate controller for the precision rotation of the motor, a type 1 transfer function model (29) was first analyzed in Matlab/Simulink[®], based on the traditional electromechanical coupled problem.

$$G_{motor}(s) = \frac{\omega(s)}{V(s)} = \frac{K_{\tau}}{JR_a s + bR_a + K_{\tau}K_b} \quad (29)$$

where K_τ represents the motor-torque constant, J represents the moment of inertia of the motor, R_a represents the armature resistance, b represents viscous friction between the shaft and bearing, and K_b represents the back-emf (electro-magnetic force) constant. The values used for the simulation are summarized in Table 4.1.

Table 4.1 Summary of Sampling Device Modeling Parameters

PARAMETER	VALUE
J	783.99 (kgm ² /rad)
b	100 (Nms/rad)
R_a	9.8 (Ohm)
K_τ	1.65E+5 (Nm/amp)
K_b	9.8E-2 (Vs/rad)

The addition of the integrator inherent to the model dynamics allows for the elimination of the steady state error in response to a step input. A PD (proportional derivative) controller (30) was chosen to add a zero to the transfer function, allowing for tunability of the transient response. The single integrator of the open-loop gain ($C \cdot G$) does not eliminate error associated with an external disturbance. To account for any significant disturbances to the system, the error can be eliminated with the use of a PI (proportional integrative) or PID (proportional integrative derivative) controllers by introducing an additionally integrator. Alternatively, the use of either a lead or lag compensators can allow researchers to maintain the error below a desired threshold.

$$C(s) = 10(1 + 0.3s) \quad (30)$$

From the analysis of the simulated responses of the system, the overall overshoot from 46% in the uncompensated system is reduced to less than 1% in the compensated system. The inherent integrator in the system dynamics eliminates the steady state error in both

systems, while the settling time is reduced to 0.06 seconds from 3 seconds (Figure 4.6) for the compensated and uncompensated systems, respectively.

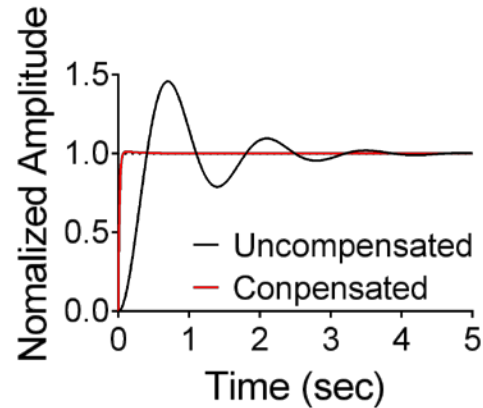


Figure 4.6 Simulated Sampling Device Motor Control

The controller was integrated into an Arduino microcontroller with desired T_{well} specified based on desired well volume and desired flow rate, Q_d . By analyzing the response of the physical system (Figure 4.7), both the settling time and overshoot remain within the design parameters at 0.3s and 1%, respectively. The response of the physical system achieves steady state within 2-degree of the desired target for the full 360° rotation indicating the presence of an external disturbance to the system, potentially from the motor belt. Because the sampling deposition is in the center of each well and is consistent at each step, the 2-degree variation has no impact on the performance of the system, because there is a 12.5-degree distance from the center to edge of a well. The increase in settling time from 0.06s to 0.3s from the simulation to physical can be attributed unmodeled nonlinear dynamics (e.g., bearing friction and belt slack) not present in our simulation. The motor dynamics were experimentally found to have a minimum settling time of 0.3s at 100% duty cycle, indicating a limitation of the overall system.

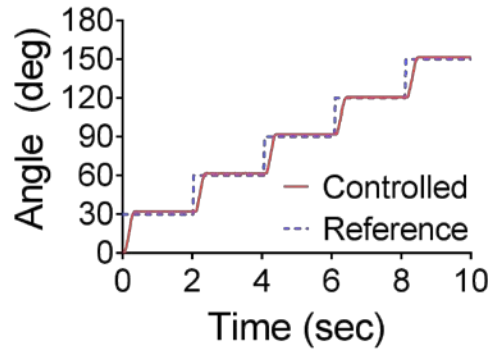


Figure 4.7 Experimental Sampling Device Controller Performance

To illustrate the effect of adding an additional integrator into the system to eliminate disturbances, a PI (proportional integrative) controller (31) was experimentally designed and evaluated. The small integrative gain (K_i) used in the controller is a result of the duty cycle control of the motor. High K_i will lead to oscillatory behavior for the first step as the integrative error is accumulated during the “windup” period. To avoid this behavior, the gain is reduced while eliminating both the oscillations and steady-state error. The steady-state error of the response is reduced from 8% to less than 2% for the PD and PI controllers, respectively. The small error observed can be a combination of the belt slack and encoder resolution. A small increase in the settling time by 0.05s using the PI controller (Figure 4.8) was observed. With the controller designed and implemented within the desired design criteria, the next step is to move forward assessing the performance of the system with fluidic sampling.

$$C(s) = \frac{(3s + 0.01)}{s} \quad (31)$$

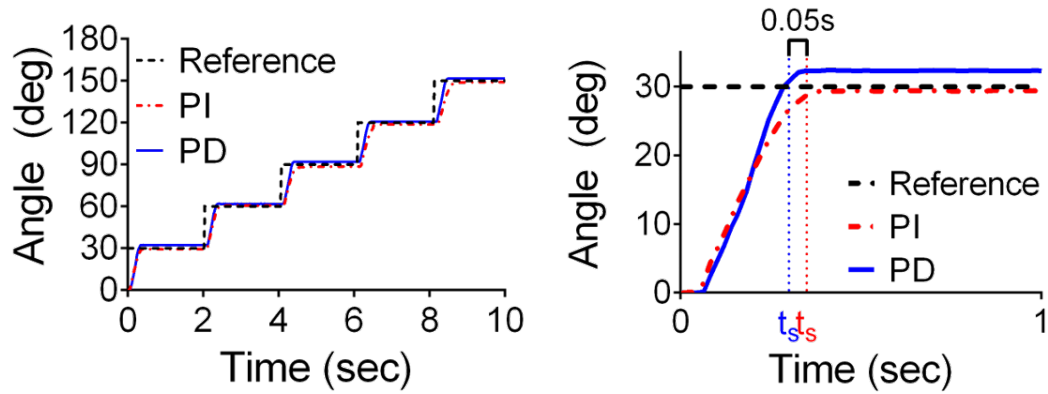


Figure 4.8 Sampling System Controller Comparison

Although the PI controller reduces the steady-state error with a slightly slower settling time, the PD controller was implemented on the physical system because of the 12.5-degree variance allowed with the microvolumetric sampler. When redesigning the microvolumetric sampler to increase the multiplicity or wells, the steady-state error may become more critical to the proper operation requiring the PI controller. To overcome the decrease in settling time and to possibly improve the steady-state error response or the PI controller, a bang-bang controller could potentially be developed but requires a more comprehensive model to appropriately design.

4.1.2 System Performance

To properly analyze the sampling performance, the constraint of connective tubing volume from the syringe pump to the sampling control device (Figure 4.9) needs to be considered. The fluidic time delay, T , is calculated from the syringe to the microvolumetric sampler based on the total volume, V_{tot} , and the desired flow rate, Q_d . For this system, the total volume was found to be approximately 200 μL with a desired flow rate of 20 $\mu\text{L}/\text{min}$, leading to a 10 min delay.

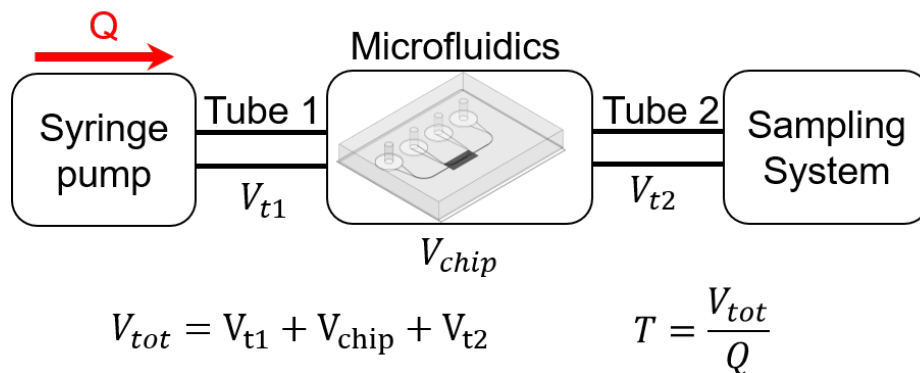


Figure 4.9 Sampling Fluidic Time Delay Diagram

To assess the accuracy of the microvolumetric sampler, the ability of the device to sample the desired volume (100 μL) at three different flow rates (i.e., 5, 20, 100 $\mu\text{L}/\text{min}$) generated by a syringe pump (Figure 4.10) was first examined. For flow rates greater than 20 $\mu\text{L}/\text{min}$, the system demonstrated high reproducibility with less than 5% error from the desired value. This discrepancy can partially be associated with the use of a needle/droplet for sampling. The formation and release of the droplet imposes a time delay on the system and by increasing the flow rate, the time delay can be reduced, achieving higher accuracy. The 5 $\mu\text{L}/\text{min}$ flow rate demonstrated a long transient time approaching the desired flow rate due to the syringe pump performance, a potential limitation of the syringe pump [89, 92, 93].

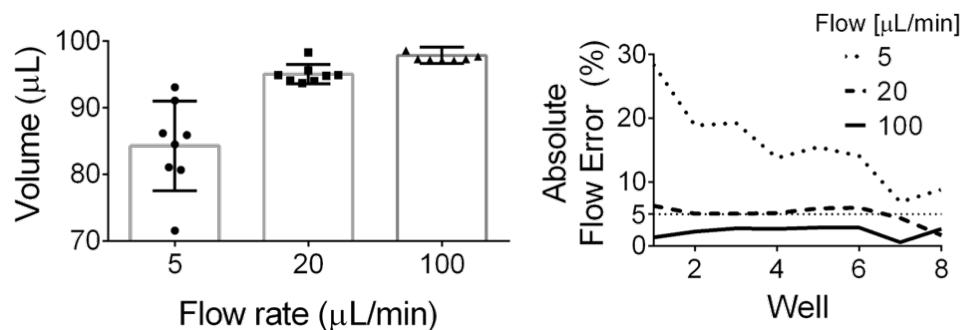


Figure 4.10 Sampling Device Accuracy Based on Flow Rate

To decrease the variability of the microvolumetric sampler, the PDMS microvolumetric sampler was oxidative plasma cleaned to create a hydrophilic surface (Figure 4.11). This allows for the sample to be wicked into the well, reducing the probability of missing the well. The sampled volume was found to have an average error of 5.86% and 2.14% for the non-plasma cleaned (control) and plasma cleaned microvolumetric sampler, respectively. The significant increase in the accuracy of the sampling volume indicates the necessity of plasma cleaning to achieve high-precision sampling.

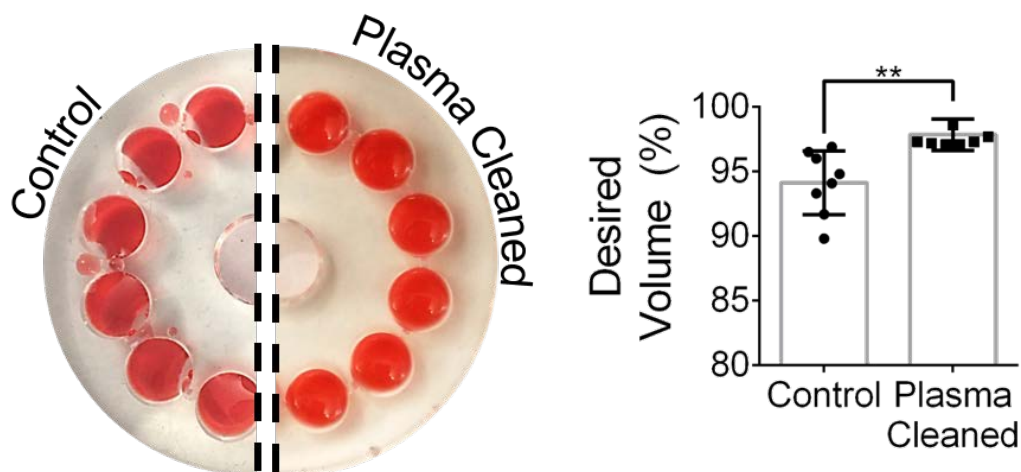


Figure 4.11 Microvolumetric Sampler Plasma Oxidation Performance

4.1.3 Continuous Sampling Approach

The approach taken for the sampling was through the discretization of the sample. Using fluidic circuit analogs and assuming each sampling well with equivalent pressure differentials, the channel dimensions of each circuit can be designed (Figure 4.12).

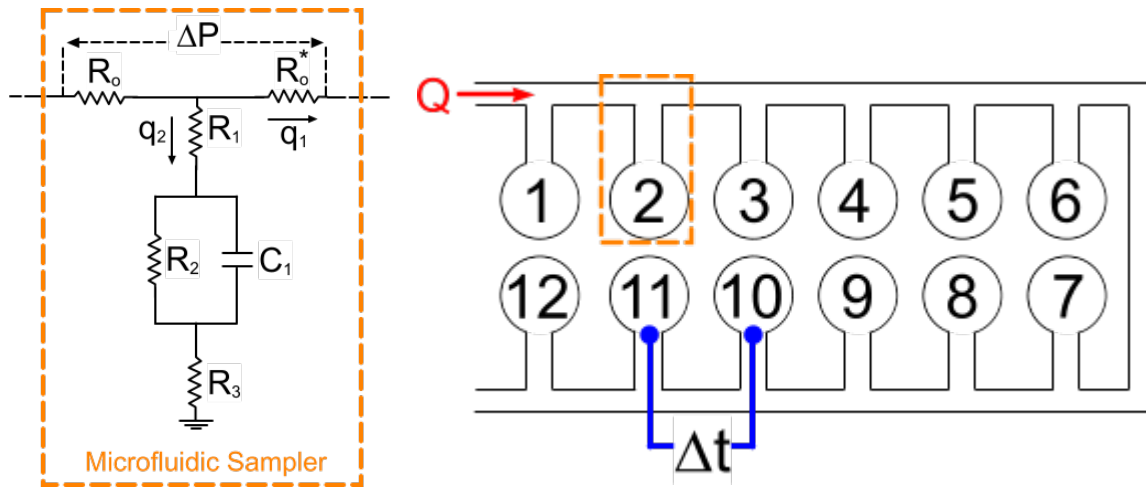


Figure 4.12 Continuous Sampling Circuit Diagram

At each of the sampling wells the fluid flow is divided between q_1 and q_2 , reducing the overall flowrate is reduced for the subsequent well. By calculating the q_2 flow rate and knowing the channel dimensions, the temporal differential between the wells can be calculated which can be tuned based on the inlet flow, Q (Figure 4.13). The design of the system is more consistent with longer experimental duration because the inverse relationship to Q makes the overall system sensitive to lower flowrates.

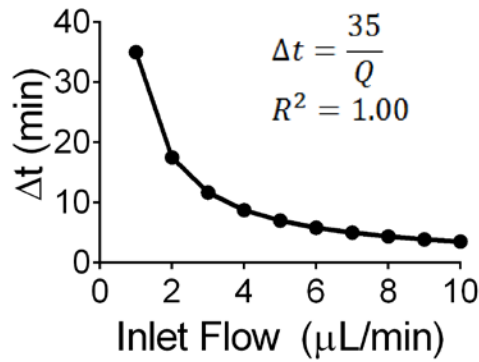


Figure 4.13 Continuous Sampling Time Differential

The constraints of the both the well volume and the temporal differential for each well increases the complexity of the design. Acting as a current divider, each of the microfluidic samplers needs to be individually designed while reducing the channel dimensions (i.e., resistances) to maintain consistent results. This process can be iteratively tuned with computational software (i.e., Matlab) by assuming parameters such as channel widths and channel height, leaving only the channel lengths to be calculated (Figure 4.14). Where the side chain length is the distance to the microfluidic well and the inter-sampler length is the distance between each microfluidic sampler. The profile of each length is nonlinear with the final value approaching a length of zero as the number of wells is increased.

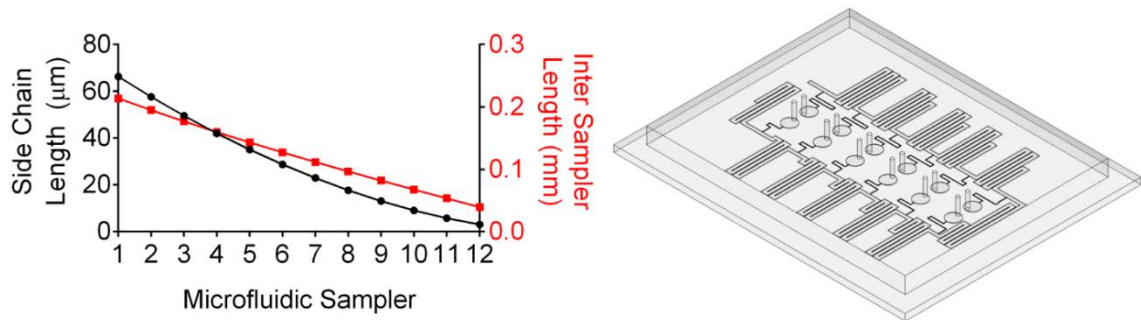


Figure 4.14 Simulated Continuous Microvolumetric Sampler Design

The continuous design, although theoretically possible, is not well suited for biological experimentation. The q_2 flowrate does not reach zero at steady-state, leading the well to have a continuous inflow of sample. This causes the first well to be a mixture of the entire experimental duration, with the final well being the initial time differential; clouding experimental results. The complexity of the design, with each well beginning individually calibrated, greatly reduces the versatility of the platform, requiring a redesign of the entire device for any change in either multiplicity of samples or volume of samples. For these reasons, the initial conceptual design was not experimentally validated, and the discretized system was developed. For the application to microfluidic systems, the discretized sampling device was integrated for experimental validation.

4.2 Application for Micro-Engineered Systems

Microfluidic sampling for biological systems is critical to high-precision and repeatable experimentation. To examine the capability of sampling with micro-engineered systems, the microvolumetric sampler device is integrated with the organ-on-a-chip device [43]. The drug/compound concentration availability across the porous membrane is, additionally, analyzed with CFD at various Re and porosities, a critical understanding for biological experiments.

4.2.1 Convective Flow Profiles

Two parallel syringe pumps, connected via a t-connection, to produce two separate flow profiles across the porous membrane (Figure 4.15). The first profile examines decrease in concentration over time, analyzing the sensitivity of the system to examine a drug/compound over a time, a critical operation for biological systems. The second profile examines the reconstitution of the drug/compound within the device, an important measure

for use of cyclic administration of dosages. Each flow profiles were examined with varied pulse of the drug/compound (i.e., 1, 2, 5, and 10 min durations), to examine the effect on longer duration effect of drug/compound availability over time and the degree to which the drug/compound concentration can be reconstituted.

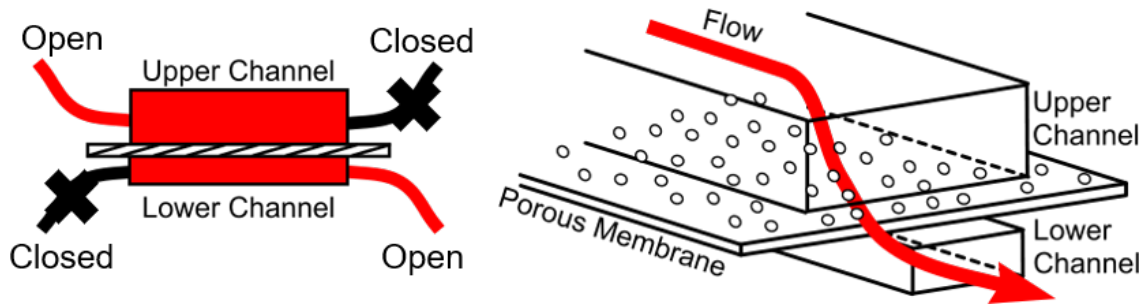


Figure 4.15 Sampling Convective Experiment Schematic

The flow rate dependability on the drug/compound availability (Figure 4.16) based on a 10 min duration of the second profile was first examined. When the flow rate is substantially increased, from Re of 2 (1x) to 35 (16x), the concentration fails to reach 0 within the same time frame. The two species of both drug/compound mix more thoroughly with the water at higher flow rates, indicating that convective mixing is occurring across the membrane. This mixing causes the time constant, to reach an equivalent 0 concentration, to be increased. At lower flow rates (i.e., Re 2), the mixing of the two species is primarily dominated by diffusion decreasing the amount of mixing between the 2 species. When considering the flow rate used in experimentation, in addition to shear stresses, cyclic drug loading is affected by flow rates, potentially modifying experimental results across repeated runs.

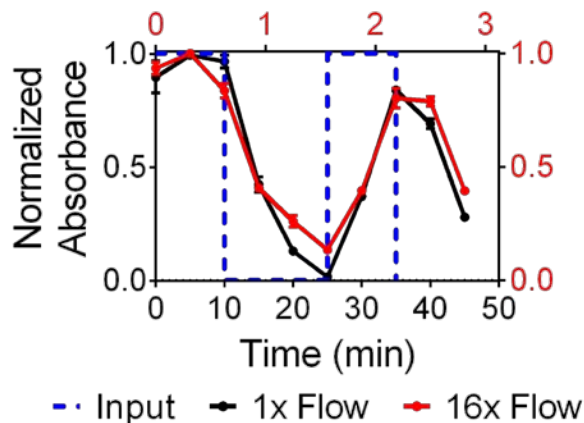


Figure 4.16 Flow Rate Comparison of Convective Experiment

To assess the effect of the various pulse durations on the reconstitution of the drug/compound concentration, the experiment was repeated with two separate concentrations (i.e., 1 and 2 mg/mL Nile Blue) at Re 2 to examine the consistency of the device at separate concentrations (Figure 4.17). Longer pulse durations demonstrated longer setting time, for the first profile, and a larger reconstitution of the drug/compound concentration, for the second profile. Increases in the concentration are consistent with the pulse input, demonstrating the sensitivity of the microvolumetric sampler device to measure the response (black) of an input profile (red). By understanding the concentration distribution over time in an organ-on-a-chip device, researchers can better model and predict drug/compound administration to cells, a critical operation for biological systems to remain physiologically relevant. By halving the concentration, the differences between the 1 and 2 min pulse negligible when observing the first profile response; however, the recovery of the drug concentration remains higher as previously observed with the full concentration. The use of 100 μ L well sizes in the microvolumetric sampler can be tuned to decrease overall volume, affecting the time per well and experiment duration. More

importantly, decreasing well size allows for a larger multiplicity of sampling that can resolve the differences between the 1 and 2 min pulse durations.

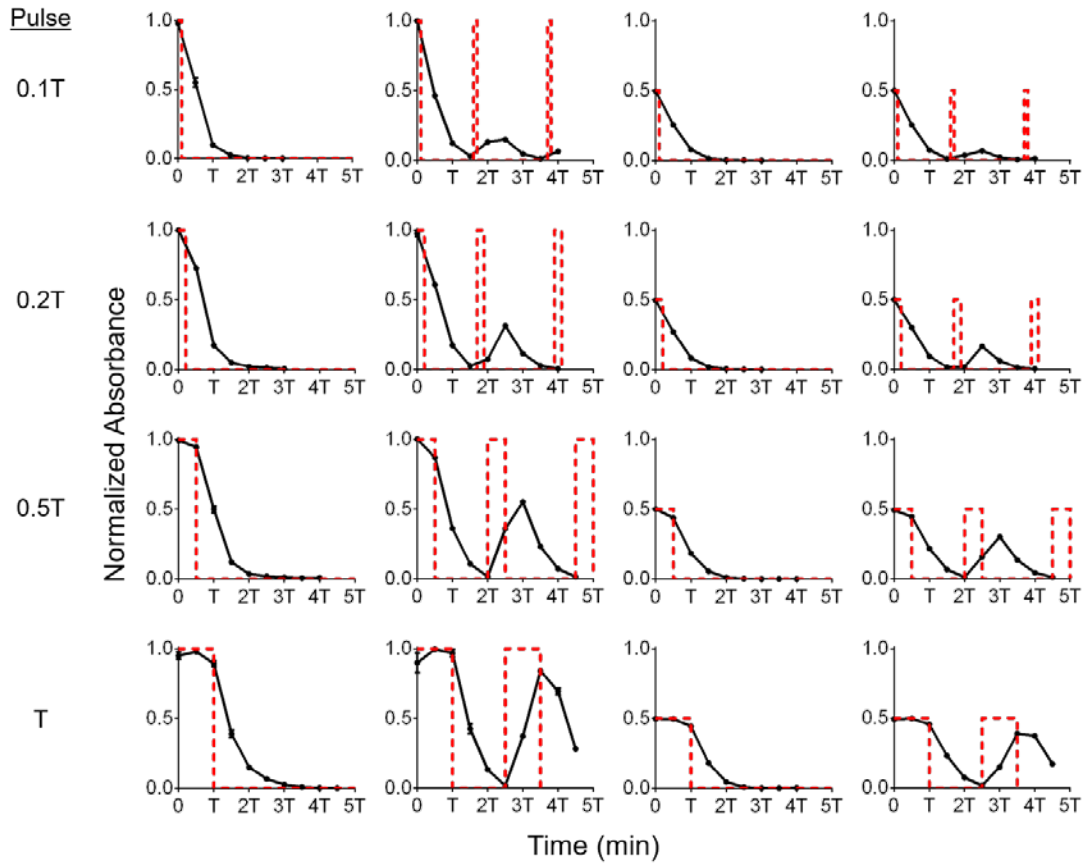


Figure 4.17 Effect of Pulse Duration on Drug/Compound Concentration

4.2.2 Static Membrane Mass Transport Simulations

To better understand the mass fraction properties within the microfluidic device, the drug/compound transport across the membrane with a static (no flow) lower channel and various Re in the upper channel (Figure 4.18 (left)) was analyzed. As the flow rate is increased in the upper channel, both the time constant and settling time of the lower channel mass fraction are decreased as the upper channel flow is increased (Figure 4.18 (right); Table 4.2).

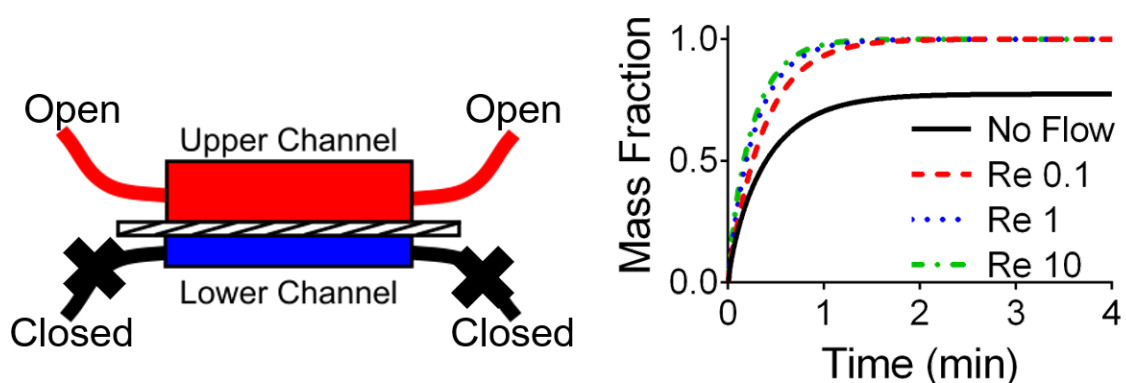


Figure 4.18 Static Membrane Diffusion Simulation

Due to the pressure differential in the upper channel to generate the various flow conditions, a pressure differential across the membrane develops, driving drug/compound from the upper to the lower channel. This phenomenon is in addition to diffusive forces acting between the two species. The larger the Re , the larger the pressure differential leading to greater flow across the membrane and faster coalescence, indicated by faster time constant and settling times. Notably, the mass fraction of the no flow condition in the upper channel reaches a steady-state value of 0.72, because there is a finite availability of drug/compound in the upper channel (e.g., static transwell). Whereas, in the flow conditions, an infinite amount of drug/compound is available allowing for a final mass fraction of 1, at steady-state (e.g., dynamic microfluidics).

Table 4.2 Simulated lower channel mass fraction analysis

UPPER CHANNEL	TIME CONSTANT	SETTLING TIME
FLOW	(MIN)	(MIN)
NO FLOW	0.38	1.63
RE 0.1	0.37	1.45
RE 1	0.28	1.16
RE 10	0.25	1.03

This analysis is essential for the defining the initial conditions of the microfluidic platforms. This is illustrated by looking at the differences between the transient responses of each upper flow condition at 20s (Figure 4.19). There is a gradual increase in the concentration of the lower channel as the flow rate is increase in the upper channel, with none of the conditions having equivalent fractions.

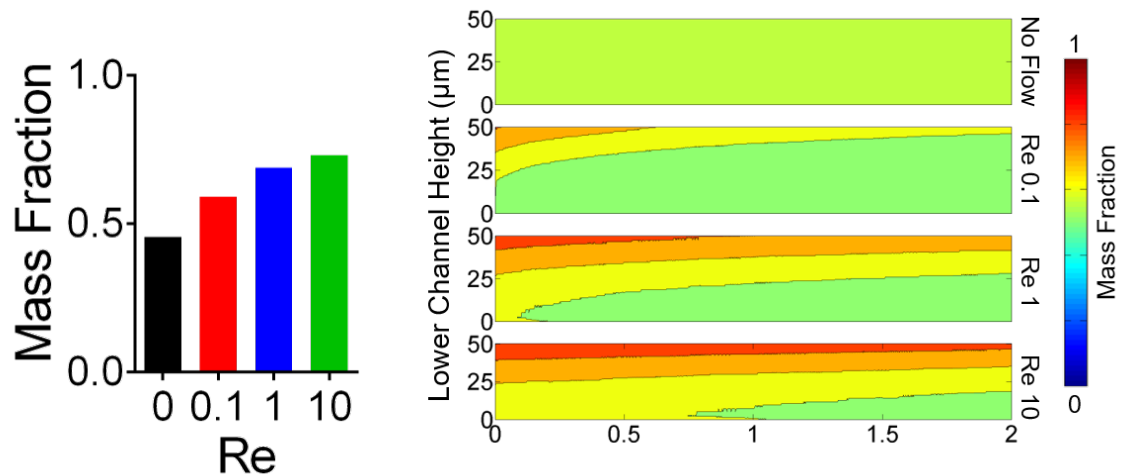


Figure 4.19 Transient Membrane Mass Transport

Increasing the time to 120s (Figure 4.20), the steady-state conditions of each of the channels with no discernable differences between the three flow cases. When designing the initial conditions of any microfluidic system, it is important to understand the effect of the

pressure differential caused between two separate channels. To continue the understanding of the mass transport of drug/compound across the membrane, the lower channel mass fraction is simulated when both the upper and lower channels have flow, causing a zero-pressure differential across the membrane and relying solely on diffusive forces for mass transport.

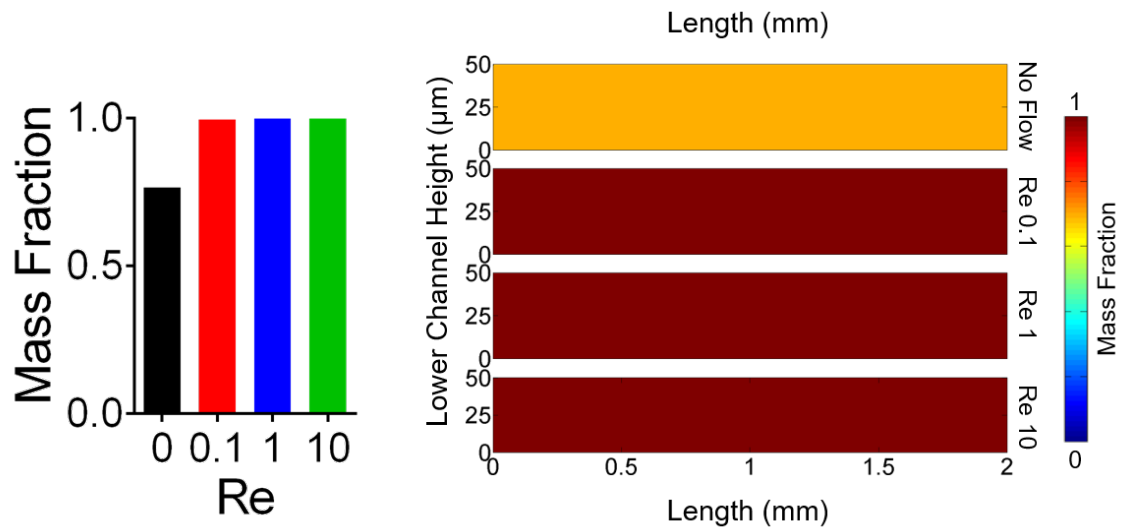


Figure 4.20 Steady-State Membrane Mass Transport

4.2.3 Membrane Porosity Effect on Mass Transport

To better understand the effect within the microfluidic device, the transport of drug/compound across the porous membrane with various Re (0.1, 1, and 10) and membrane porosity (0.05, 0.5, and 1) by creating simultaneously flows in the upper and lower channels (Figure 4.21) was modeled.

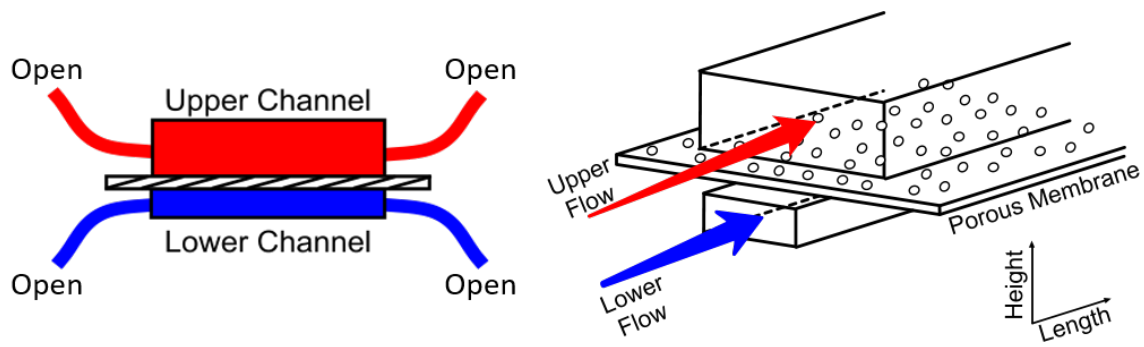


Figure 4.21 Membrane Porosity Mass Transport Simulation Schematic

Examining the effect of the porosity of the membrane (Figure 4.22), it was observed that as the porosity decreased, indicative of a higher resistance to flow, the concentration of the lower channel decreases at steady-state. This is consistent with an electrical analog characterization of the membrane through the Hagan-Poiseuille equation [88], where the higher resistance impedes flow given equivalent pressure differentials. To better observe the properties with regards to cellular applications, the mass fraction to the Re, shear stress, and flow rate are compared. By increasing the porosity of the membrane, the transition in the mass fraction was found to be nonlinear with higher sensitivity at higher porosities. The average shear stress for arterioles and capillaries is on the range of 40-60 dyne/cm² and lower in large arteries and venules, on the range of 10-20 dyne/cm² [134]. For the device used, this is on the range of Re of 2 to 3 for the large arteries and venules. Due to the nonlinear nature of the mass fraction at various porosities, to generate physiologically relevant studies it is critical to analyze the membrane's effect on the mass fraction to ensure proper drug/compound administration.

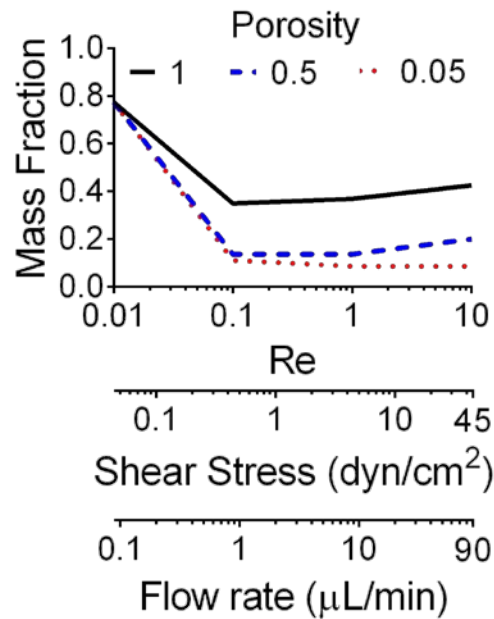


Figure 4.22 Lower Channel Steady-State Mass Fraction

Analyzing the effect of the Re on the lower channel mass fraction, longer transient times due to the bulk flow overcoming the diffusive forces (Figure 4.23) when Re is increased are observed. Interestingly, although the flow was calculated to eliminate a pressure differential between the upper and lower channels, for the porosities of 1 and 0.5 the overall concentration is increased as the Re increased. This indicates that the upper and lower pressure differentials may not be equivalent, generating a flow across the membrane. Whereas when the porosity is decreased to 0.05, no flow across the membrane occurs because the resistance is large enough to impede flow and diffusive forces become dominant. The flow and membrane properties are an integral part to properly developing biological microfluidic systems, to ensure proper administration of drug/compounds.

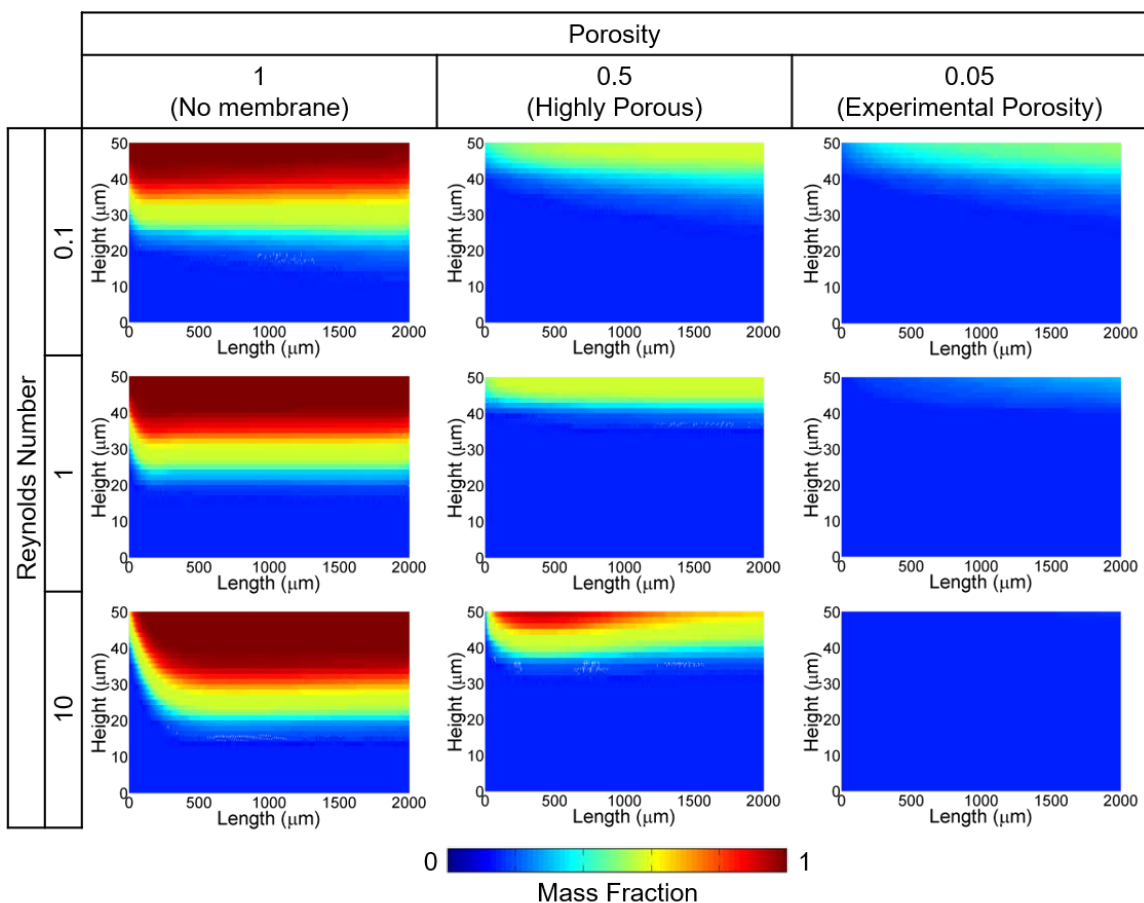


Figure 4.23 Lower Channel Mass Fraction Distribution

4.3 Conclusions

A tunable low-cost high-precision sampling device for integration with microfluidics through a feedback-controlled microvolumetric sampler has been developed. The robust controller design, including the versatility of the microvolumetric sampler design, and the necessity of plasma cleaning for optimal performance were demonstrated. The sensitivity of the sampling device was assessed to evaluate proper administration of drugs/compounds, and the system was shown to be able to respond to a desired input profile. The drug/compound concentration of both the porosity of the membrane and the Re of the fluid through computational analysis were evaluated, finding a necessity to

examine membrane properties because of nonlinear behavior and convective mixing attributed to membrane porosity. The tunable high-precision sampling device and computational analysis of membrane properties can be used to improve organ-on-a-chip studies, mimicking physiologically relevant values, while providing versatility for a broader range of applications including chemical synthesis, nanoparticle formation, and other microfluidic studies.

Chapter 5 Denouement

The fields of micro-engineered biological systems and the pursuit of new nanotherapeutics have garnered increasing attention over the last few decades. A current challenge of these fields is that they are generally reliant on chemists, biologists, and other aspects of life sciences to design and develop these platforms. Considerably less attention has been drawn to the use of engineers and, more importantly, engineering principles for microfluidics and biological applications. This work demonstrates, not only, the potential of combining the two fields but demonstrates the advantages over solely biology approaches. The engineering principles applied here can be broadened to aspects beyond the areas of pressure control, parallelization, and sampling, to the design of new microfluidic platforms or design modular microfluidic platforms. This integration allows for precision designed microfluidic channels for various applications which can be used to develop microfluidic logic gates or complicated integrated fluidic circuits.

Broader Impact

The work demonstrated here is not only limited to the applications that have been presented, giving researchers versatility. The feedback pressure control system can be broadened beyond use for microfluidic nanoparticle synthesis, to be able to control organ-on-a-chip flow. The ability to prescribe an arbitrary pressure input profile allows for researchers to have the versatility to pursue various flow conditions and recreate physiologically relevant flows (e.g., ventricle pressure curves for vasculature-on-a-chip or pulmonary artery-on-a-chip). The pressure range of the profile is dependent on the pressure sensor integrated in the system, and, by changing out the sensor, researchers can customize both the range and resolution of the pressure response can be adjusted. This only

requires the PI controller to be tuned, ensuring similar performance to the work demonstrated in Chapter 2.

The parallelized microfluidic array developed in Chapter 3 can be extended to devices beyond the swirling microvortex reactor (SMR). The method of analyzing the critical components to nanoparticle size and quality to design about applies to any microfluidic nanoparticle platform. The limitation of only 2-inlets was not widely discussed, but the simplicity of the design was because of the 2-inlet SMR. Extending the device to 3 or more inlets does not require a large redesign or a new complicated model. Because the SMR inlet resistance is over a thousand-fold increase over the outlet resistance, the inter-inlet sensitivity is essentially negligible [135]. Maintaining this property for 3 or more inlets allows researchers to stack PMA systems on top of one another, with rotations, to obtain 4 or 6 inlet devices. Each layer would require additional gaskets and to allow for numerous connections, the distance between the reactors needs to potentially be increased. By increasing the microfluidic reactor channel lengths, the $Z_2:Z_3$ ratio needs to be considered, maintaining reactor consistency.

Being able to design for multi-inlet microfluidics, opens the possibility of modularity for large scale manufacturing. Creating a universal outlet and parallelized network design, the system can be designed to switch out the microfluidic device. For an arbitrary design, the generalized microfluidic width and length create a design constraint on the parallelization. This simplifies the process for using platforms not necessarily for LPNP as described in Chapter 3 but for either other NP or chemical syntheses, and from a manufacturing perspective, saves overall cost by minimizing the required or components needing to be fabricated.

The sampling device developed in Chapter 4 can be integrated with any microfluidic platform from the organ-on-a-chip device discussed or for even NP synthesis. The device can be further refined to include a 3-way actuated valve to sample in discretized intervals as opposed to the continuous model presented. This adds increasing complexity to ensure the proper volume and time point are deposited into the well because of the dead volume within the valve and, in this case, needle connection. This can be overcome by clearing the dead volume with either water or a new sample, but in either case the sample properties are skewed through mixing of the two separate species. This additionally requires a modified control algorithm to rotate to a waste well, potentially effecting system performance. For long term experimental duration, sample evaporation can potentially lead to experimental variation and needs to be assessed for other applications.

Overall, each of the methods and technologies here can be expanded far beyond what was developed in this work allowing for versatility. By using the tools and understanding each of the principles used to develop each platform, the technology can be modified while maintaining the superior performance. Achieving a cross between classical engineering principles and biological platforms, the work will continue to evolve and accelerate the advancement of each field.

References

- [1] A. Z. Wang, R. Langer, and O. C. Farokhzad, "Nanoparticle delivery of cancer drugs," *Annual review of medicine*, vol. 63, pp. 185-198, 2012.
- [2] M. E. Davis and D. M. Shin, "Nanoparticle therapeutics: an emerging treatment modality for cancer," *Nature reviews Drug discovery*, vol. 7, no. 9, pp. 771-782, 2008.
- [3] R. Bazak, M. Houri, S. El Achy, S. Kamel, and T. Refaat, "Cancer active targeting by nanoparticles: a comprehensive review of literature," *Journal of cancer research and clinical oncology*, vol. 141, no. 5, pp. 769-784, 2015.
- [4] B. L. Chung *et al.*, "Nanomedicines for endothelial disorders," *Nano Today*, 2016.
- [5] K. Donaldson *et al.*, "Nanoparticles and the cardiovascular system: a critical review," *Nanomedicine*, vol. 8, no. 3, pp. 403-423, 2013.
- [6] O. Veisheh, B. C. Tang, K. A. Whitehead, D. G. Anderson, and R. Langer, "Managing diabetes with nanomedicine: challenges and opportunities," *Nature Reviews Drug Discovery*, vol. 14, no. 1, pp. 45-57, 2015.
- [7] G. Sharma, A. R. Sharma, J.-S. Nam, G. P. Doss, S.-S. Lee, and C. Chakraborty, "Nanoparticle based insulin delivery system: the next generation efficient therapy for Type 1 diabetes," *Journal of nanobiotechnology*, vol. 13, no. 1, p. 74, 2015.
- [8] M. Huang *et al.*, "GM1-Modified Lipoprotein-like Nanoparticle: Multifunctional Nanoplatfrom for the Combination Therapy of Alzheimer's Disease," *ACS nano*, vol. 9, no. 11, pp. 10801-10816, 2015.
- [9] E. Muntimadugu, R. Dhommatti, A. Jain, V. G. S. Challa, M. Shaheen, and W. Khan, "Intranasal delivery of nanoparticle encapsulated tarenflurbil: A potential brain targeting strategy for Alzheimer's disease," *European Journal of Pharmaceutical Sciences*, 2016.
- [10] N. Gao, H. Sun, K. Dong, J. Ren, and X. Qu, "Gold-Nanoparticle-Based Multifunctional Amyloid- β Inhibitor against Alzheimer's Disease," *Chemistry-A European Journal*, vol. 21, no. 2, pp. 829-835, 2015.
- [11] D. Bobo, K. J. Robinson, J. Islam, K. J. Thurecht, and S. R. Corrie, "Nanoparticle-Based Medicines: A Review of FDA-Approved Materials and Clinical Trials to Date," *Pharmaceutical research*, pp. 1-15, 2016.
- [12] H. F. Chan, S. Ma, and K. W. Leong, "Can microfluidics address biomanufacturing challenges in drug/gene/cell therapies?," *Regenerative biomaterials*, p. rbw009, 2016.
- [13] N. Desai, "Challenges in development of nanoparticle-based therapeutics," *The AAPS journal*, vol. 14, no. 2, pp. 282-295, 2012.
- [14] P. M. Valencia, O. C. Farokhzad, R. Karnik, and R. Langer, "Microfluidic technologies for accelerating the clinical translation of nanoparticles," *Nature nanotechnology*, vol. 7, no. 10, pp. 623-629, 2012.
- [15] J.-M. Lim *et al.*, "Parallel microfluidic synthesis of size-tunable polymeric nanoparticles using 3D flow focusing towards in vivo study," *Nanomedicine: Nanotechnology, Biology and Medicine*, vol. 10, no. 2, pp. 401-409, 2014.
- [16] D. Liu, S. Cito, Y. Zhang, C. F. Wang, T. M. Sikanen, and H. A. Santos, "A versatile and robust microfluidic platform toward high throughput synthesis of

- homogeneous nanoparticles with tunable properties," *Advanced Materials*, vol. 27, no. 14, pp. 2298-2304, 2015.
- [17] Y. Kim and R. Langer, "Microfluidics in Nanomedicine," *Reviews in Cell Biology and Molecular Medicine*, 2015.
 - [18] Y. Song, J. Hormes, and C. S. Kumar, "Microfluidic synthesis of nanomaterials," *Small*, vol. 4, no. 6, pp. 698-711, 2008.
 - [19] M. Rhee, P. M. Valencia, M. I. Rodriguez, R. Langer, O. C. Farokhzad, and R. Karnik, "Synthesis of Size-Tunable Polymeric Nanoparticles Enabled by 3D Hydrodynamic Flow Focusing in Single-Layer Microchannels," *Advanced Materials*, vol. 23, no. 12, pp. H79-H83, 2011.
 - [20] J. Sun *et al.*, "A microfluidic origami chip for synthesis of functionalized polymeric nanoparticles," *Nanoscale*, vol. 5, no. 12, pp. 5262-5265, 2013.
 - [21] J. Sun *et al.*, "Tunable rigidity of (polymeric core)–(lipid shell) nanoparticles for regulated cellular uptake," *Advanced Materials*, vol. 27, no. 8, pp. 1402-1407, 2015.
 - [22] R. Othman, G. T. Vladislavljević, H. H. Bandulasena, and Z. K. Nagy, "Production of polymeric nanoparticles by micromixing in a co-flow microfluidic glass capillary device," *Chemical Engineering Journal*, vol. 280, pp. 316-329, 2015.
 - [23] I. V. Zhigaltsev *et al.*, "Bottom-up design and synthesis of limit size lipid nanoparticle systems with aqueous and triglyceride cores using millisecond microfluidic mixing," *Langmuir*, vol. 28, no. 7, pp. 3633-3640, 2012.
 - [24] M. Mizuno, T. Toyota, M. Konishi, Y. Kageyama, M. Yamada, and M. Seki, "Formation of monodisperse hierarchical lipid particles utilizing microfluidic droplets in a nonequilibrium state," *Langmuir*, vol. 31, no. 8, pp. 2334-2341, 2015.
 - [25] Y. Kim *et al.*, "Mass production and size control of lipid–polymer hybrid nanoparticles through controlled microvortices," *Nano letters*, vol. 12, no. 7, pp. 3587-3591, 2012.
 - [26] Y. Kim *et al.*, "Single step reconstitution of multifunctional high-density lipoprotein-derived nanomaterials using microfluidics," *ACS Nano*, vol. 7, no. 11, pp. 9975-83, Nov 26 2013.
 - [27] Y. Kim and R. Langer, "Microfluidics in nanomedicine," in *Reviews in Cell Biology and Molecular Medicine*, vol. 1, R. A. Meyers, Ed.: Wiley-VCH Verlag GmbH & Co. KGaA., 2015, pp. 127-152.
 - [28] A. J. Mieszawska *et al.*, "Synthesis of polymer-lipid nanoparticles for image-guided delivery of dual modality therapy," *Bioconjug Chem*, vol. 24, no. 9, pp. 1429-34, Sep 18 2013.
 - [29] S. Hornig, T. Heinze, C. R. Becer, and U. S. Schubert, "Synthetic polymeric nanoparticles by nanoprecipitation," *Journal of Materials Chemistry*, vol. 19, no. 23, pp. 3838-3840, 2009.
 - [30] E. Sollier, C. Murray, P. Maoddi, and D. Di Carlo, "Rapid prototyping polymers for microfluidic devices and high pressure injections," *Lab on a Chip*, vol. 11, no. 22, pp. 3752-3765, 2011.
 - [31] R. H. Fang, K. N. Chen, S. Aryal, C.-M. J. Hu, K. Zhang, and L. Zhang, "Large-scale synthesis of lipid–polymer hybrid nanoparticles using a multi-inlet vortex reactor," *Langmuir*, vol. 28, no. 39, pp. 13824-13829, 2012.

- [32] J.-M. Lim *et al.*, "Ultra-high throughput synthesis of nanoparticles with homogeneous size distribution using a coaxial turbulent jet mixer," *ACS nano*, vol. 8, no. 6, pp. 6056-6065, 2014.
- [33] T. Nisisako and T. Torii, "Microfluidic large-scale integration on a chip for mass production of monodisperse droplets and particles," *Lab on a Chip*, vol. 8, no. 2, pp. 287-293, 2008.
- [34] M. B. Romanowsky, A. R. Abate, A. Rotem, C. Holtze, and D. A. Weitz, "High throughput production of single core double emulsions in a parallelized microfluidic device," *Lab on a chip*, vol. 12, no. 4, pp. 802-807, 2012.
- [35] M. K. Mulligan and J. P. Rothstein, "Scale-up and control of droplet production in coupled microfluidic flow-focusing geometries," *Microfluidics and nanofluidics*, vol. 13, no. 1, pp. 65-73, 2012.
- [36] G. T. Vladislavljjevic *et al.*, "Industrial lab-on-a-chip: design, applications and scale-up for drug discovery and delivery," *Adv Drug Deliv Rev*, vol. 65, no. 11-12, pp. 1626-63, Nov 2013.
- [37] N. M. Belliveau *et al.*, "Microfluidic synthesis of highly potent limit-size lipid nanoparticles for in vivo delivery of siRNA," *Molecular Therapy—Nucleic Acids*, vol. 1, no. 8, p. e37, 2012.
- [38] R. R. Hood and D. L. DeVoe, "High-Throughput Continuous Flow Production of Nanoscale Liposomes by Microfluidic Vertical Flow Focusing," *small*, vol. 11, no. 43, pp. 5790-5799, 2015.
- [39] D. Huh, B. D. Matthews, A. Mammoto, M. Montoya-Zavala, H. Y. Hsin, and D. E. Ingber, "Reconstituting organ-level lung functions on a chip," *Science*, vol. 328, no. 5986, pp. 1662-1668, 2010.
- [40] H. J. Kim and D. E. Ingber, "Gut-on-a-Chip microenvironment induces human intestinal cells to undergo villus differentiation," *Integrative Biology*, vol. 5, no. 9, pp. 1130-1140, 2013.
- [41] Y. Kim *et al.*, "Probing nanoparticle translocation across the permeable endothelium in experimental atherosclerosis," *Proceedings of the National Academy of Sciences*, vol. 111, no. 3, pp. 1078-1083, 2014.
- [42] M. J. Wilmer, C. P. Ng, H. L. Lanz, P. Vulto, L. Suter-Dick, and R. Masereeuw, "Kidney-on-a-chip technology for drug-induced nephrotoxicity screening," *Trends in biotechnology*, vol. 34, no. 2, pp. 156-170, 2016.
- [43] Y. J. Sei, S. I. Ahn, T. Virtue, T. Kim, and Y. Kim, "Detection of frequency-dependent endothelial response to oscillatory shear stress using a microfluidic transcellular monitor," *Scientific Reports*, vol. 7, no. 1, p. 10019, 2017/08/30 2017.
- [44] V. Tesař, "Sampling by fluidics and microfluidics," *Acta Polytechnica*, vol. 42, no. 2, 2002.
- [45] K. S. Elvira, X. C. i Solvas, and R. C. Wootton, "The past, present and potential for microfluidic reactor technology in chemical synthesis," *Nature chemistry*, vol. 5, no. 11, pp. 905-915, 2013.
- [46] C. A. Schütz, L. Juillerat-Jeanneret, H. Mueller, I. Lynch, and M. Riediker, "Therapeutic nanoparticles in clinics and under clinical evaluation," *Nanomedicine*, vol. 8, no. 3, pp. 449-467, 2013.
- [47] C. M. Hovell, Y. J. Sei, and Y. Kim, "Microengineered vascular systems for drug development," *Journal of laboratory automation*, p. 2211068214560767, 2014.

- [48] J. Wu, Q. Chen, W. Liu, Z. He, and J.-M. Lin, "Recent advances in microfluidic 3D cellular scaffolds for drug assays," *TrAC Trends in Analytical Chemistry*, vol. 87, pp. 19-31, 2017.
- [49] I. L. Medintz, H. T. Uyeda, E. R. Goldman, and H. Mattoussi, "Quantum dot bioconjugates for imaging, labelling and sensing," *Nature materials*, vol. 4, no. 6, pp. 435-446, 2005.
- [50] M.-C. Daniel and D. Astruc, "Gold nanoparticles: assembly, supramolecular chemistry, quantum-size-related properties, and applications toward biology, catalysis, and nanotechnology," *Chemical reviews*, vol. 104, no. 1, pp. 293-346, 2004.
- [51] S. Zeng, K.-T. Yong, I. Roy, X.-Q. Dinh, X. Yu, and F. Luan, "A review on functionalized gold nanoparticles for biosensing applications," *Plasmonics*, vol. 6, no. 3, pp. 491-506, 2011.
- [52] A. K. Gupta and M. Gupta, "Synthesis and surface engineering of iron oxide nanoparticles for biomedical applications," *Biomaterials*, vol. 26, no. 18, pp. 3995-4021, 2005.
- [53] R. Kuai, D. Li, Y. E. Chen, J. J. Moon, and A. Schwendeman, "High-Density Lipoproteins: Nature's Multifunctional Nanoparticles," *ACS nano*, vol. 10, no. 3, pp. 3015-3041, 2016.
- [54] Y. Malam, M. Loizidou, and A. M. Seifalian, "Liposomes and nanoparticles: nanosized vehicles for drug delivery in cancer," *Trends in pharmacological sciences*, vol. 30, no. 11, pp. 592-599, 2009.
- [55] J. J. Bergers, T. L. ten Hagen, E. W. van Etten, and I. A. Bakker-Woudenberg, "Liposomes as delivery systems in the prevention and treatment of infectious diseases," *Pharmacy world and science*, vol. 17, no. 1, pp. 1-11, 1995.
- [56] M. Elsabahy and K. L. Wooley, "Design of polymeric nanoparticles for biomedical delivery applications," *Chemical Society Reviews*, vol. 41, no. 7, pp. 2545-2561, 2012.
- [57] C. P. Reis, R. J. Neufeld, A. J. Ribeiro, and F. Veiga, "Nanoencapsulation I. Methods for preparation of drug-loaded polymeric nanoparticles," *Nanomedicine: Nanotechnology, Biology and Medicine*, vol. 2, no. 1, pp. 8-21, 2006.
- [58] K. Hadinoto, A. Sundaresan, and W. S. Cheow, "Lipid-polymer hybrid nanoparticles as a new generation therapeutic delivery platform: a review," *European Journal of Pharmaceutics and Biopharmaceutics*, vol. 85, no. 3, pp. 427-443, 2013.
- [59] O. V. Salata, "Applications of nanoparticles in biology and medicine," *Journal of nanobiotechnology*, vol. 2, no. 1, p. 3, 2004.
- [60] M. Hans and A. Lowman, "Biodegradable nanoparticles for drug delivery and targeting," *Current Opinion in Solid State and Materials Science*, vol. 6, no. 4, pp. 319-327, 2002.
- [61] M. Athar and A. J. Das, "Therapeutic nanoparticles: State-of-the-art of nanomedicine," *Adv. Mater. Rev*, vol. 1, no. 1, pp. 25-37, 2014.
- [62] K. S. Soppimath, T. M. Aminabhavi, A. R. Kulkarni, and W. E. Rudzinski, "Biodegradable polymeric nanoparticles as drug delivery devices," *Journal of controlled release*, vol. 70, no. 1, pp. 1-20, 2001.

- [63] C.-X. Zhao and A. P. Middelberg, "Synthesis and Characterization of Nanomaterials Using Microfluidic Technology," *Handbook of Nanoparticles*, pp. 455-473, 2016.
- [64] A. Kumari, S. K. Yadav, and S. C. Yadav, "Biodegradable polymeric nanoparticles based drug delivery systems," *Colloids and Surfaces B: Biointerfaces*, vol. 75, no. 1, pp. 1-18, 2010.
- [65] R. Singh and J. W. Lillard, "Nanoparticle-based targeted drug delivery," *Experimental and molecular pathology*, vol. 86, no. 3, pp. 215-223, 2009.
- [66] J. M. Harris and R. B. Chess, "Effect of pegylation on pharmaceuticals," *Nature Reviews Drug Discovery*, vol. 2, no. 3, pp. 214-221, 2003.
- [67] F. M. Veronese and G. Pasut, "PEGylation, successful approach to drug delivery," *Drug discovery today*, vol. 10, no. 21, pp. 1451-1458, 2005.
- [68] L. Zhang *et al.*, "self-assembled lipid–polymer hybrid nanoparticles: a robust drug delivery platform," *ACS nano*, vol. 2, no. 8, pp. 1696-1702, 2008.
- [69] B. Mandal *et al.*, "Core–shell-type lipid–polymer hybrid nanoparticles as a drug delivery platform," *Nanomedicine: Nanotechnology, Biology and Medicine*, vol. 9, no. 4, pp. 474-491, 2013.
- [70] A. M. Ghaemmaghami, M. J. Hancock, H. Harrington, H. Kaji, and A. Khademhosseini, "Biomimetic tissues on a chip for drug discovery," *Drug discovery today*, vol. 17, no. 3, pp. 173-181, 2012.
- [71] H. Song and R. F. Ismagilov, "Millisecond kinetics on a microfluidic chip using nanoliters of reagents," *Journal of the American Chemical Society*, vol. 125, no. 47, pp. 14613-14619, 2003.
- [72] M. W. Losey, R. J. Jackman, S. L. Firebaugh, M. Schmidt, and K. F. Jensen, "Design and fabrication of microfluidic devices for multiphase mixing and reaction," *Microelectromechanical Systems, Journal of*, vol. 11, no. 6, pp. 709-717, 2002.
- [73] S. M. Mitrovski, L. C. Elliott, and R. G. Nuzzo, "Microfluidic devices for energy conversion: Planar integration and performance of a passive, fully immersed H₂-O₂ fuel cell," *Langmuir*, vol. 20, no. 17, pp. 6974-6976, 2004.
- [74] G. M. Whitesides, "The origins and the future of microfluidics," *Nature*, vol. 442, no. 7101, pp. 368-373, 2006.
- [75] J. M. Chan *et al.*, "PLGA–lecithin–PEG core–shell nanoparticles for controlled drug delivery," *Biomaterials*, vol. 30, no. 8, pp. 1627-1634, 2009.
- [76] T. Govender, S. Stolnik, M. C. Garnett, L. Illum, and S. S. Davis, "PLGA nanoparticles prepared by nanoprecipitation: drug loading and release studies of a water soluble drug," *Journal of Controlled Release*, vol. 57, no. 2, pp. 171-185, 1999.
- [77] R. Seemann, M. Brinkmann, T. Pfohl, and S. Herminghaus, "Droplet based microfluidics," *Reports on progress in physics*, vol. 75, no. 1, p. 016601, 2012.
- [78] S.-Y. Teh, R. Lin, L.-H. Hung, and A. P. Lee, "Droplet microfluidics," *Lab on a Chip*, vol. 8, no. 2, pp. 198-220, 2008.
- [79] T. M. Squires and S. R. Quake, "Microfluidics: Fluid physics at the nanoliter scale," *Reviews of modern physics*, vol. 77, no. 3, p. 977, 2005.

- [80] A. Liao, R. Karnik, A. Majumdar, and J. H. D. Cate, "Mixing crowded biological solutions in milliseconds," *Analytical chemistry*, vol. 77, no. 23, pp. 7618-7625, 2005.
- [81] L.-H. Hung, K. M. Choi, W.-Y. Tseng, Y.-C. Tan, K. J. Shea, and A. P. Lee, "Alternating droplet generation and controlled dynamic droplet fusion in microfluidic device for CdS nanoparticle synthesis," *Lab on a Chip*, vol. 6, no. 2, pp. 174-178, 2006.
- [82] T. Stiles *et al.*, "Hydrodynamic focusing for vacuum-pumped microfluidics," *Microfluidics and Nanofluidics*, vol. 1, no. 3, pp. 280-283, 2005.
- [83] R. Karnik *et al.*, "Microfluidic platform for controlled synthesis of polymeric nanoparticles," *Nano letters*, vol. 8, no. 9, pp. 2906-2912, 2008.
- [84] M. J. Toth, T. Kim, and Y. Kim, "Robust manufacturing of lipid-polymer nanoparticles through feedback control of parallelized swirling microvortices," (in English), *Lab on a Chip*, vol. 17, no. 16, pp. 2805-2813, Aug 21 2017.
- [85] W. Li *et al.*, "Simultaneous generation of droplets with different dimensions in parallel integrated microfluidic droplet generators," *Soft matter*, vol. 4, no. 2, pp. 258-262, 2008.
- [86] Y. Zeng, R. Novak, J. Shuga, M. T. Smith, and R. A. Mathies, "High-performance single cell genetic analysis using microfluidic emulsion generator arrays," *Analytical chemistry*, vol. 82, no. 8, pp. 3183-3190, 2010.
- [87] T. Nisisako, T. Ando, and T. Hatsuzawa, "High-volume production of single and compound emulsions in a microfluidic parallelization arrangement coupled with coaxial annular world-to-chip interfaces," *Lab on a Chip*, vol. 12, no. 18, pp. 3426-3435, 2012.
- [88] K. W. Oh, K. Lee, B. Ahn, and E. P. Furlani, "Design of pressure-driven microfluidic networks using electric circuit analogy," *Lab on a Chip*, vol. 12, no. 3, pp. 515-545, 2012.
- [89] W. Zeng, I. Jacobi, D. J. Beck, S. Li, and H. A. Stone, "Characterization of syringe-pump-driven induced pressure fluctuations in elastic microchannels," *Lab on a Chip*, vol. 15, no. 4, pp. 1110-1115, 2015.
- [90] Z. Li, S. Y. Mak, A. Sauret, and H. C. Shum, "Syringe-pump-induced fluctuation in all-aqueous microfluidic system implications for flow rate accuracy," *Lab on a Chip*, vol. 14, no. 4, pp. 744-749, 2014.
- [91] G. M. Walker and D. J. Beebe, "A passive pumping method for microfluidic devices," *Lab on a Chip*, vol. 2, no. 3, pp. 131-134, 2002.
- [92] H. A. Stone, A. D. Stroock, and A. Ajdari, "Engineering flows in small devices: microfluidics toward a lab-on-a-chip," *Annu. Rev. Fluid Mech.*, vol. 36, pp. 381-411, 2004.
- [93] M. Martin, G. Blu, C. Eon, and G. Guiochon, "The use of syringe-type pumps in liquid chromatography in order to achieve a constant flow-rate," *Journal of Chromatography A*, vol. 112, pp. 399-414, 1975.
- [94] J. Lee, F. Rahman, T. Laoui, and R. Karnik, "Bubble-induced damping in displacement-driven microfluidic flows," *Physical Review E*, vol. 86, no. 2, p. 026301, 2012.
- [95] Y. J. Kang and S. Yang, "Fluidic low pass filter for hydrodynamic flow stabilization in microfluidic environments," *Lab on a Chip*, vol. 12, no. 10, pp. 1881-1889, 2012.

- [96] R.-L. Chien and W. J. Parce, "Multiport flow-control system for lab-on-a-chip microfluidic devices," *Fresenius' journal of analytical chemistry*, vol. 371, no. 2, pp. 106-111, 2001.
- [97] B. Kuczenski, P. R. LeDuc, and W. C. Messner, "Pressure-driven spatiotemporal control of the laminar flow interface in a microfluidic network," *Lab on a Chip*, vol. 7, no. 5, pp. 647-649, 2007.
- [98] J. L. Lima, J. L. Santos, A. C. Dias, M. F. Ribeiro, and E. A. Zagatto, "Multi-pumping flow systems: an automation tool," *Talanta*, vol. 64, no. 5, pp. 1091-1098, 2004.
- [99] J. Ruzicka, G. D. Marshall, and G. D. Christian, "Variable flow rates and a sinusoidal flow pump for flow injection analysis," *Analytical chemistry*, vol. 62, no. 17, pp. 1861-1866, 1990.
- [100] C. Fütterer *et al.*, "Injection and flow control system for microchannels," *Lab on a Chip*, vol. 4, no. 4, pp. 351-356, 2004.
- [101] R. A. Lapa, J. L. Lima, B. F. Reis, J. L. Santos, and E. A. Zagatto, "Multi-pumping in flow analysis: concepts, instrumentation, potentialities," *Analytica Chimica Acta*, vol. 466, no. 1, pp. 125-132, 2002.
- [102] J. S. Fitch, A. K. Henning, E. B. Arkilic, and J. M. Harris, "Pressure-based mass-flow control using thermopneumatically-actuated microvalves," in *Proceedings, Sensors and Actuators Workshop*, 1998, pp. 162-165.
- [103] J. D. Tice, A. V. Desai, T. A. Bassett, C. A. Appleby, and P. J. Kenis, "Control of pressure-driven components in integrated microfluidic devices using an on-chip electrostatic microvalve," *RSC Advances*, vol. 4, no. 93, pp. 51593-51602, 2014.
- [104] E. F. Hasselbrink, T. J. Shepodd, and J. E. Rehm, "High-pressure microfluidic control in lab-on-a-chip devices using mobile polymer monoliths," *Analytical Chemistry*, vol. 74, no. 19, pp. 4913-4918, 2002.
- [105] D. J. Beebe *et al.*, "Functional hydrogel structures for autonomous flow control inside microfluidic channels," *Nature*, vol. 404, no. 6778, pp. 588-590, 2000.
- [106] Y. Kim, P. LeDuc, and W. Messner, "Modeling and control of a nonlinear mechanism for high performance microfluidic systems," *Control Systems Technology, IEEE Transactions on*, vol. 21, no. 1, pp. 203-211, 2013.
- [107] Y. Kim, B. Kuczenski, P. R. LeDuc, and W. C. Messner, "Modulation of fluidic resistance and capacitance for long-term, high-speed feedback control of a microfluidic interface," *Lab on a Chip*, vol. 9, no. 17, pp. 2603-2609, 2009.
- [108] A. Jain, A. Graveline, A. Waterhouse, A. Vernet, R. Flaumenhaft, and D. E. Ingber, "A shear gradient-activated microfluidic device for automated monitoring of whole blood haemostasis and platelet function," *Nature communications*, vol. 7, p. 10176, 2016.
- [109] M. A. Unger, H.-P. Chou, T. Thorsen, A. Scherer, and S. R. Quake, "Monolithic microfabricated valves and pumps by multilayer soft lithography," *Science*, vol. 288, no. 5463, pp. 113-116, 2000.
- [110] W. H. Grover, R. H. Ivester, E. C. Jensen, and R. A. Mathies, "Development and multiplexed control of latching pneumatic valves using microfluidic logical structures," *Lab on a Chip*, vol. 6, no. 5, pp. 623-631, 2006.

- [111] J. A. Weaver, J. Melin, D. Stark, S. R. Quake, and M. A. Horowitz, "Static control logic for microfluidic devices using pressure-gain valves," (in English), *Nature Physics*, vol. 6, no. 3, pp. 218-223, Mar 2010.
- [112] X. Li, J. C. Brooks, J. Hu, K. I. Ford, and C. J. Easley, "3D-templated, fully automated microfluidic input/output multiplexer for endocrine tissue culture and secretion sampling," *Lab on a Chip*, vol. 17, no. 2, pp. 341-349, 2017.
- [113] T. Thorsen, S. J. Maerkl, and S. R. Quake, "Microfluidic large-scale integration," *Science*, vol. 298, no. 5593, pp. 580-4, Oct 18 2002.
- [114] I. E. Araci and S. R. Quake, "Microfluidic very large scale integration (mVLSI) with integrated micromechanical valves," *Lab on a Chip*, vol. 12, no. 16, pp. 2803-2806, 2012.
- [115] T. Schneider, J. Kreutz, and D. T. Chiu, "The potential impact of droplet microfluidics in biology," *Analytical chemistry*, vol. 85, no. 7, pp. 3476-3482, 2013.
- [116] S. Mashaghi, A. Abbaspourrad, D. A. Weitz, and A. M. van Oijen, "Droplet microfluidics: A tool for biology, chemistry and nanotechnology," *TrAC Trends in Analytical Chemistry*, vol. 82, pp. 118-125, 2016.
- [117] T. R. Slaney *et al.*, "Push-pull perfusion sampling with segmented flow for high temporal and spatial resolution in vivo chemical monitoring," *Analytical chemistry*, vol. 83, no. 13, pp. 5207-5213, 2011.
- [118] S. Feng, G. Liu, L. Jiang, Y. Zhu, E. M. Goldys, and D. W. Inglis, "A microfluidic needle for sampling and delivery of chemical signals by segmented flows," *Applied Physics Letters*, vol. 111, no. 18, p. 183702, 2017.
- [119] A. Sposito and D. L. DeVoe, "Staggered Trap Arrays for Robust Microfluidic Sample Digitization," *Lab on a Chip*, 2017.
- [120] A. Mephram, J. Besant, A. Weinstein, I. Burgess, E. Sargent, and S. Kelley, "Power-free, digital and programmable dispensing of picoliter droplets using a Digit Chip," *Lab on a Chip*, vol. 17, no. 8, pp. 1505-1514, 2017.
- [121] M. Tomizuka, "Zero phase error tracking algorithm for digital control," *Journal of Dynamic Systems, Measurement, and Control*, vol. 109, no. 1, pp. 65-68, 1987.
- [122] Y. Kim *et al.*, "Mechanochemical actuators of embryonic epithelial contractility," *Proceedings of the National Academy of Sciences*, vol. 111, no. 40, pp. 14366-14371, 2014.
- [123] Y. Sei, K. Justus, P. LeDuc, and Y. Kim, "Engineering living systems on chips: from cells to human on chips," *Microfluidics and nanofluidics*, vol. 16, no. 5, pp. 907-920, 2014.
- [124] Y. Kim, S. D. Joshi, W. C. Messner, P. R. LeDuc, and L. A. Davidson, "Detection of dynamic spatiotemporal response to periodic chemical stimulation in a *Xenopus* embryonic tissue," *PloS one*, vol. 6, no. 1, p. e14624, 2011.
- [125] Y. Kim *et al.*, "Single step reconstitution of multifunctional high-density lipoprotein-derived nanomaterials using microfluidics," *Acs Nano*, vol. 7, no. 11, pp. 9975-9983, 2013.
- [126] J. P. Brody, P. Yager, R. E. Goldstein, and R. H. Austin, "Biotechnology at low Reynolds numbers," *Biophysical journal*, vol. 71, no. 6, pp. 3430-3441, 1996.
- [127] Y. Wang *et al.*, "Biomimetic HDL nanoparticle mediated tumor targeted delivery of indocyanine green for enhanced photodynamic therapy," *Colloids and Surfaces B: Biointerfaces*, vol. 148, pp. 533-540, 2016.

- [128] C. Vitali, C. L. Wellington, and L. Calabresi, "HDL and cholesterol handling in the brain," *Cardiovascular research*, vol. 103, no. 3, pp. 405-413, 2014.
- [129] D. A. Bricarello, J. T. Smilowitz, A. M. Zivkovic, J. B. German, and A. N. Parikh, "Reconstituted lipoprotein: a versatile class of biologically-inspired nanostructures," *ACS Nano*, vol. 5, no. 1, pp. 42-57, Jan 25 2011.
- [130] J. Ahn, Y. J. Sei, N. L. Jeon, and Y. Kim, "Probing the effect of bioinspired nanomaterials on angiogenic sprouting using a microengineered vascular system," *IEEE Transactions on Nanotechnology*, 2017.
- [131] A. Y. Shih, S. G. Sligar, and K. Schulten, "Maturation of high-density lipoproteins," *Journal of The Royal Society Interface*, p. rsif20090173, 2009.
- [132] J. C. Kraft, J. P. Freeling, Z. Wang, and R. J. Ho, "Emerging research and clinical development trends of liposome and lipid nanoparticle drug delivery systems," *Journal of pharmaceutical sciences*, vol. 103, no. 1, pp. 29-52, 2014.
- [133] P. Pradhan, J. Guan, D. Lu, P. G. Wang, L. J. Lee, and R. J. Lee, "A facile microfluidic method for production of liposomes," *Anticancer research*, vol. 28, no. 2A, pp. 943-947, 2008.
- [134] K. H. Wong, J. M. Chan, R. D. Kamm, and J. Tien, "Microfluidic models of vascular functions," *Annual review of biomedical engineering*, vol. 14, pp. 205-230, 2012.
- [135] Y. Kim, "Closed-loop microfluidic control for probing multicellular dynamics," Carnegie Mellon University, 2011.